J. metamorphic Geol., 2009, **27**, 439–459 doi:10.1111/j.1525-1314.2009.00827.x

Exhumation during oblique transpression: The Feiran–Solaf region, Egypt

T. S. ABU-ALAM AND K. STÜWE
Institut für Erdwissenschaften, Universität Graz, Universitätsplatz 2, A-8010 Graz, Austria (tamer.abu-alam@uni-graz.at)

ABSTRACT The Feiran–Solaf metamorphic complex of Sinai, Egypt, is one of the highest grade metamorphic complexes of a series of basement domes that crop out throughout the Arabian-Nubian Shield. In the Eastern Desert of Egypt these basement domes have been interpreted as metamorphic core complexes exhumed in extensional settings. For the Feiran–Solaf complex an interpretation of the exhumation mechanism is difficult to obtain with structural arguments as all of its margins are obliterated by post-tectonic granites. Here, metamorphic methods are used to investigate its tectonic history and show that the complex was characterized by a single metamorphic cycle experiencing peak metamorphism at ~700–750 °C and 7–8 kbar and subsequent isothermal decompression to ~4–5 kbar, followed by near isobaric cooling to 450 °C. Correlation of this metamorphic evolution with the deformation history shows that peak metamorphism occurred prior to the compressive deformation phase D_2, while the compressive D_2 and D_3 deformation occurred during the near isothermal decompression phase of the P–T loop. We interpret the concurrence of decompression of the P–T path and compression by structural shortening as evidence for the Najd fault system exhuming the complex in an oblique transpressive regime. However, final exhumation from ~15 km depth must have occurred due to an unrelated mechanism.

Key words: deformation phases; exhumation process; Pan-African Orogeny; P–T–D path; thermodynamic modelling.

INTRODUCTION

The Sinai Peninsula is the northern segment of the Arabian-Nubian Shield, which comprises the northern part of the East African Orogen. The East African Orogen was assembled by accretion of an intraoceanic island arc system associated with the closing of the Mozambique Ocean during the Neoproterozoic (Engel *et al.*, 1980; Gass, 1982; Kröner, 1984; Kröner *et al.*, 1994; Fritz *et al.*, 1996, 2002; Katz *et al.*, 2004). The entire arc assembly was then thrust during the Pan-African orogeny over a cratonic, gneissic basement, which is exposed in a series of tectonic windows throughout northern Africa and Arabian Peninsula (Fig. 1). This basement is often considered to be of much older age than the arc assembly (El-Gaby *et al.*, 1990). A lack of knowledge regarding the relationship between the low-grade arc assembly and the much higher grade basement units underneath severely limits our ability to reconstruct the tectonic evolution of this region (Stern & Manton, 1987).

One way to constrain this relationship is by studying the metamorphic evolution of the gneissic basement and correlating this with the structural events that covered and later exhumed the gneisses from underneath the arc assembly. Such studies have been performed in several of the gneissic windows in the Eastern Desert of Egypt (e.g. Meatiq and Sibai core complexes, Fritz *et al.*, 2002) and also in Sinai (e.g. Kid area: Abu El-Enen *et al.*, 2003; Blasband *et al.*, 1997, 2000; Brooijmans *et al.*, 2003; Eliwa *et al.*, 2008; Taba area: Abu El-Enen *et al.*, 2004; Eliwa *et al.*, 2008). These studies have shown that the basement domes may be high grade equivalents of the low-grade arc assembly, and that some of these domes are core complexes in the classic sense. Several of these studies have also shown that the exhumation of the gneiss domes is associated with the activity of a major (more than 1000 km long and hundreds of km wide) NW–SE striking sinistral shear zone system called the Najd fault system (Fig. 1). However, one of the highest grade complexes in Egypt and the largest metamorphic one in Sinai has not been studied metamorphically and its exhumation history has not been explained: the Feiran–Solaf metamorphic complex (FSMC) (Fig. 2). This complex constitutes a narrow strip of gneisses in the northwestern part of the exposed igneous and metamorphic rocks in Sinai.

El-Gaby & Ahmed (1980) recognized that the FSMC is made up of two asymmetric doubly-plunging antiforms, namely the Feiran antiform and the Solaf antiform, separated by synformal trough. This geometry suggests that the FSMC may be a core complex similar to those of the Eastern Desert of Egypt (e.g. Fritz *et al.*, 1996, 2002; Loizenbauer *et al.*, 2001; Abd El-Naby *et al.*, 2008; Khudeir *et al.*, 2008), but we will show here that this is not the case.

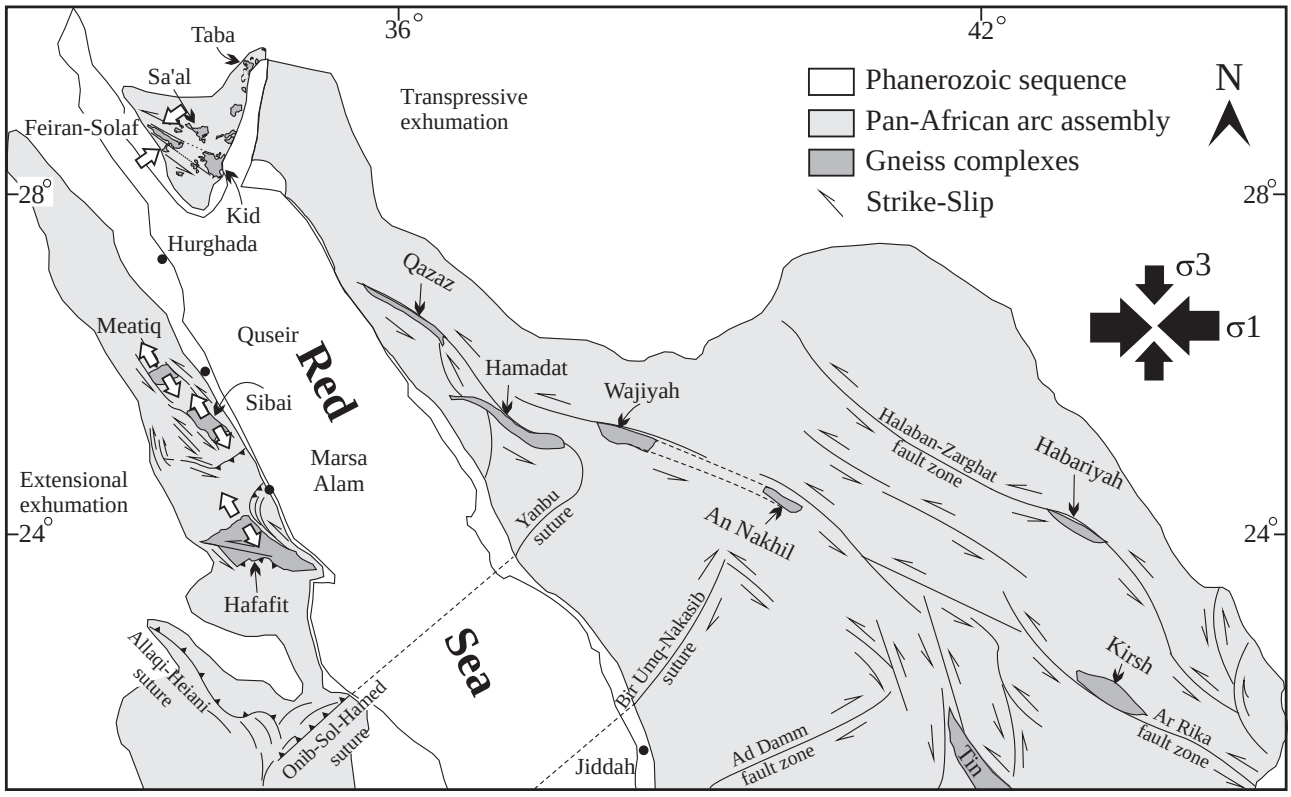

Fig. 1. Metamorphic gneiss complexes, Najd fault system and sutures of the northern part of the Arabian-Nubian Shield. Black arrows show principal stress directions for the Najd fault system as a whole. Small white arrows show strain in individual gneiss complexes. Note that this is extensional in the Eastern desert, but transpressive in the Feiran–Solaf metamorphic complex. (Complied from various sources, including: Abdelsalam & Stern, 1996; Fritz *et al*., 1996; Johnson, 1998).

This study investigates the metamorphic evolution of Feiran–Solaf complex to constrain the tectonic evolution of the area. A mineral equilibria approach is used with petrogenetic pseudosections and relate the derived metamorphic history to the detailed structural map and structural evolution derived by El-Shafei & Kusky (2003). Our tectonic model is then correlated with independent field evidence, existing geochronological ages from the region and with other gneiss domes elsewhere in the Arabian-Nubian Shield.

GEOLOGICAL SETTING

The FSMC is a NW trending elongate folded belt ~40 km long and 5–11 km wide (Fig. 2) parallel to the orientation of the Najd fault system. It is made up of migmatitic biotite and hornblende gneisses, quartzofeldspathic gneisses and hornblende gneisses with subordinate schists, amphibolite and calcsilicate rocks. The complex was intruded and surrounded by a number of granitic plutons, including pre-, syn- to post-tectonic granitoids, diorite and large volumes of dykes with mafic to felsic composition. These intrusions obliterate all structural relationships along the margins of the complex. The northwestern part of the complex is covered by Phanerozoic sedimentary rocks. The complex can be divided into two zones: the Feiran zone in the north-west and the Solaf zone in the south-east. These two zones are separated by a diorite intrusion (Fig. 2). The Feiran zone contains migmatitic biotite and hornblende gneisses, hornblende gneisses, quartzofeldspathic gneisses and locally some dolerites. In contrast, the Solaf zone is mostly composed of quartzofeldspathic gneisses (with very minor bands of metagraywackes but with mappable portions of calcsilicate rocks; Fig. 2). There are also less abundant granitic gneisses and amphibolites as small lenses and pockets.

The rock units in the entire complex are systematically arranged around two doubly-plunging antiformal structures: The Feiran antiform in the north-west and the Solaf antiform in the south-east (Fig. 2). Stern & Manton (1988) suggested that a thrust fault separates the two antiforms, but El-Shafei & Kusky (2003) found no evidence for such a fault. Migmatitic biotite and hornblende gneisses occur in the core of the structure, the hornblende gneisses structurally above and the quartzofeldspathic gneisses above those. The calcsilicates generally appear to be located in the structurally highest levels. This arrangement has been interpreted as a stratigraphic succession by Ahmed (1981). El-Gaby & Ahmed (1980) interpreted the Feiran

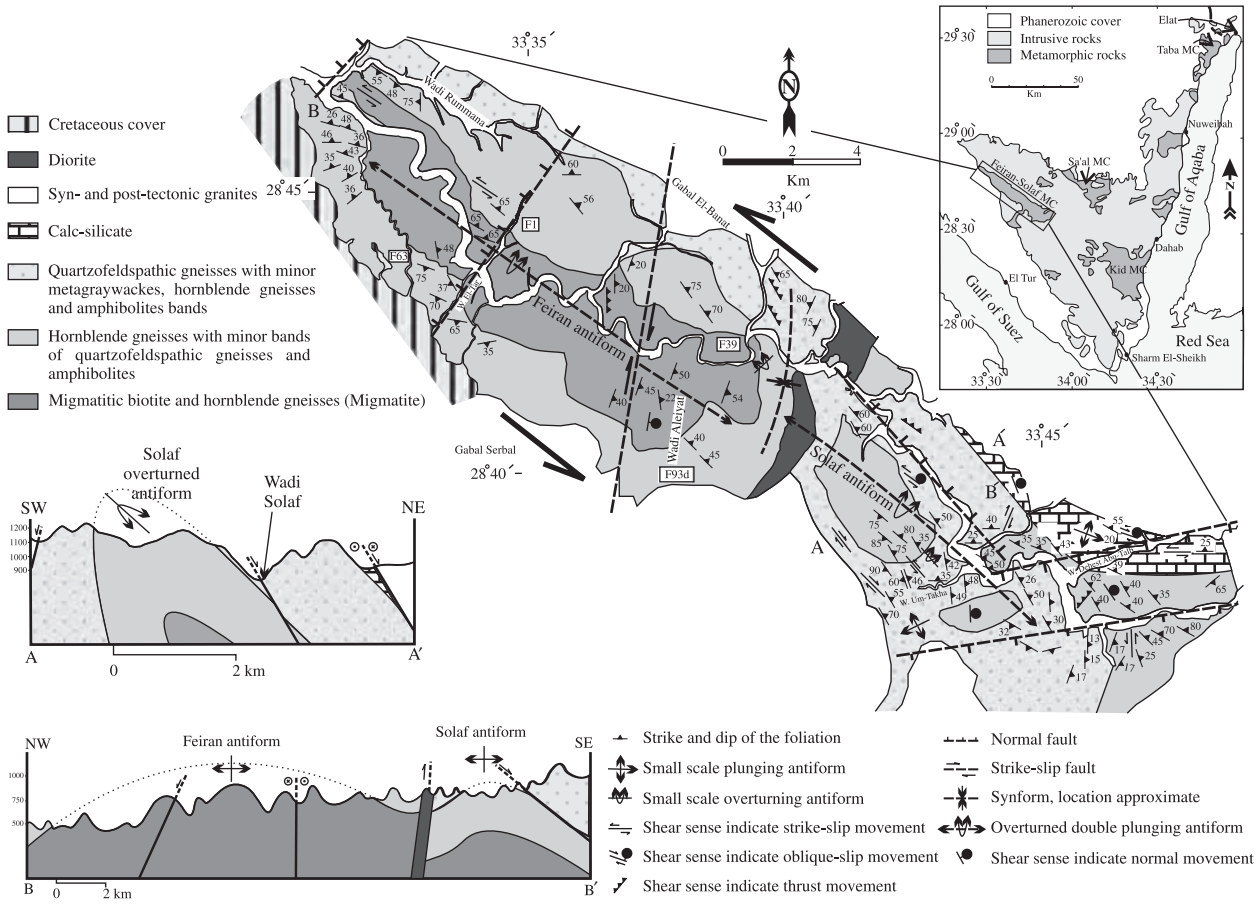

Fig. 2. Location map (MC, metamorphic complex) and simplified geological map of the Feiran–Solaf metamorphic complex. Contacts are modified from Ahmed (1981); El-Shafei & Kusky (2003) and Fowler & Hassan (2008). The white squares are the sample locations (F1, F63, F93d & F39). Structural cross-sections, A–A′ through the Solaf zone and B–B′ are drawn sub-parallel to the main fold axes of the Feiran and the Solaf antiforms. Lithological changes are often gradational and the mapped contacts are therefore approximate.

gneisses to represent a thick (> 5000 m) sedimentary succession with minor mafic intercalations. Several authors have observed that metamorphism in the FSMC appears to increase towards the core of the structure, i.e. towards deeper structural levels. In the migmatitic biotite and hornblende gneisses, the metamorphic grade is reported to have reached upper amphibolite facies conditions from 640 to 700 °C at pressure from 4 to 5 kbar during the Pan-African Orogeny (e.g. Eliwa *et al.*, 2008). A zircon age derived by Stern & Manton (1987) suggests 632 ± 3 Ma for the high-grade migmatitic event. A K–Ar biotite cooling age (Eliwa *et al.*, 2008) suggests 617–594 Ma as the time of cooling and exhumation.

Structure and kinematics

Most authors agree that the history of the Pan-African deformation in Sinai can be described in terms of four Proterozoic deformation phases D_1–D_4 (e.g. Eliwa *et al.*, 2008), where D_1 is the primary foliation forming event interpreted to be related to an early Pan-African extensional environment. D_2 and D_3 are shortening phases forming the large scale geometry of the metamorphic complexes and D_4 is a gentle warping event. For the FSMC, Fowler & Hassan (2008) suggested that the major doubly-plunging antiforms building the map scale geometry of the complex were formed during D_3 (Fig. 2). As this is a somewhat different interpretation from that of El-Shafei & Kusky (2003), a summary of the structural evolution is presented based on the literature and our own data below.

The earliest structure observed in the FSMC is the primary lithological layering termed S_0. Lithological bands are from < 1 cm to several metres in thickness and are defined mainly by variation in the amounts and type of mafic minerals. Good examples of this primary lithological layering (S_0) are thin continuous layers of amphibolite (Fig. 3a) and calcsilicate rock within quartzofeldspathic gneisses (Fowler & Hassan, 2008).

Fowler & Hassan (2008) as well as El-Shafei & Kusky (2003) suggested that the dominant metamorphic foliation in the FSMC is S_1. While this nomenclature is retained here, we note that Abu El-Enen

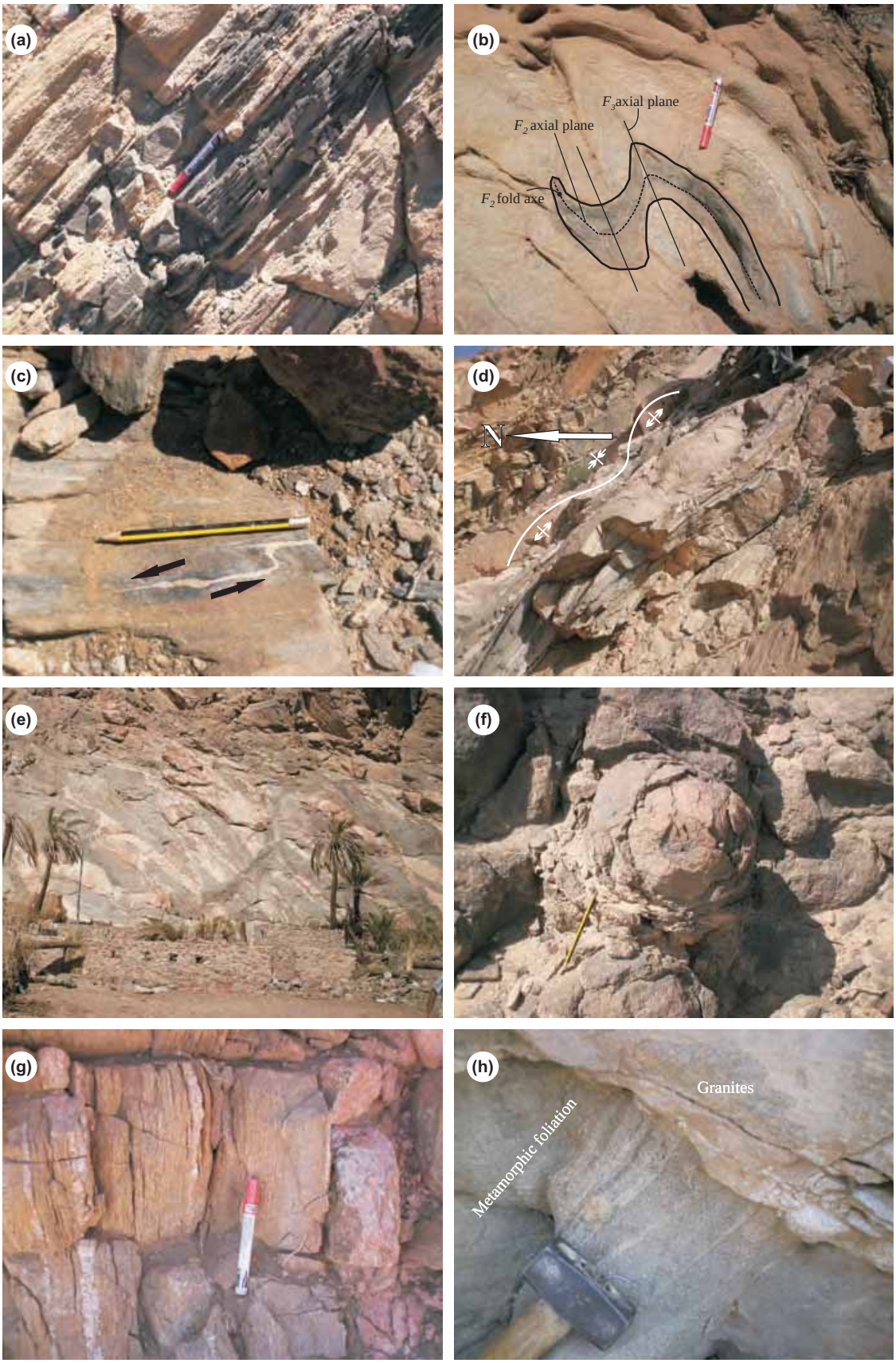

et al. (2003, 2004) suggested that the main foliation forming event in the Taba and Kid belts of Sinai is D_2. Indeed, we found remnants of an earlier fabric as inclusion trails in garnet in the FSMC. Nevertheless, as these inclusion trails are rare, the main foliation event is termed D_1, keeping in mind that earlier phases may have occurred.

D_1 formed a strong stretching lineation and intrafolial F_1-folds generally trending NW–SE. Shear sense indicators indicate west and north-west directed transport but Fowler & Hassan (2008) showed that the principal strain during this event was vertical flattening with stretching in both NW–SE and NE–SW directions. They also suggested that this extensional D_1 reflected the larger-scale extension related to the breakup of Rodinia. In contrast, El-Shafei & Kusky (2003) inferred that D_1 was responsible for the map scale geometry of the FSMC. However, because the S_1 foliation is wrapped around the hinges of the map scale antiforms, we follow here Fowler & Hassan (2008) and suggest that the map scale geometry must be related to later deformation phases.

The D_2 phase formed tight folds (F_2) (Fig. 3b) occasionally associated with a crenulation cleavage (S_2). The F_2-folds commonly refold F_1-folds. These structures are well preserved in the Solaf zone along Wadi Solaf. The F_2-folds trend parallel to the F_1 trends (NW–SE and NNW–SSE) and clearly formed due to shortening in NE–SW direction. Because F_1 and F_2 axes are largely parallel, El-Shafei & Kusky (2003) interpreted F_1 and F_2 to be both related to the same deformation phase D_1.

The third deformation phase D_3 formed inclined open folds (F_3) causing the map scale structure of the complex and the Feiran and the Solaf antiforms (Fowler & Hassan, 2008). El-Shafei & Kusky (2003) interpreted this phase to be related to the Najd fault system and associated it with NW–SE sinistral strike–slip shear zones. These sinistral movements are well recorded along the entire study area (Fig. 3c) and well preserved in the calcsilicates. The F_3 hinges are roughly parallel to the F_1 and the F_2 hinges trending shallowly (NW–SE and NNW–SSE) parallel to the regional trend of the map scale antiforms. The F_3-folds commonly refold F_2-folds (Fig. 3b).

The D_4 deformation phase is an open warping event that domed up the entire area and is associated with NNW–trending quartz veins and gashes. F_4-folds are extremely rare and trend NE–SW, ENE–WSW and E–W (Fig. 3d). The best example of an F_4-fold is the NE–SW synformal trough which separates the Feiran and the Solaf antiforms (Fig. 2). The presence of NNW-trending quartz veins and the gashes indicates extension in NE–SW direction. It is possible that D_3 (shear zones along the margins of the complex) and D_4 are responsible for the exhumation of the region. However, this is difficult to infer in the field as the post- and syn-tectonic D_4 granitic bodies surround the entire complex and obliterate all of its margins. Some strong deformation features are developed along the margins of the metamorphic complex, but these are apparently related to the intrusion of the syn-tectonic granites. For example, horizontal flattening shows both sinistral and dextral movements and is especially found at the end of Wadi Um-Takha and in the calcsilicate rocks at the end of Wadi Dehest Abu-Talb (Fig. 2 SE end of study region). During the Red Sea and the Suez Gulf rifting, the entire study area was deformed by brittle extensional structural features. These features appear clearly as dyke swarms with Phanerozoic age (e.g. Ahmed & Youssef, 1976; El-Shafei & Kusky, 2003) and dextral strike–slip faults. The best example of these faults is the fault which cuts Gabal El-Banat and Gabal Serbal (post-tectonic granites) (Fig. 2).

Lithologies

Most rocks of the FSMC are quartzofeldspathic paragneisses with or without hornblende and with or without migmatitic features. Aluminous metasediments are rare. Stern & Manton (1987) suggested that the protoliths of the Feiran gneisses were probably very immature, volcanogenic wackes or perhaps lithic arenites inter-bedded with felsic tuffs.

The migmatitic biotite and hornblende gneisses (henceforth called 'migmatites') (Fig. 3e) in the core of Feiran zone are metatexites formed due to partial melting (El-Shafei & Kusky, 2003). They are composed of quartzofeldspathic leucosomes containing minor biotite and hornblende and hornblende-rich mesosomes containing minor biotite. In general, the migmatites are pyroxene-free rocks, but rare pyroxene-bearing migmatites occur. Complex structural patterns are observed; include stromatic, folded stromatic, ptygmatic and schlieren structures. The characteristic feature of the migmatites is the abundance of leucosomes that occur both layer parallel and cross-cutting to the principal foliation (S_1). The migmatites are intercalated with hornblende gneisses and

Fig. 3. Field photographs. (a) Two conformably inter-bedded amphibolite bands parallel to the sedimentary relict bedding of the paragneisses in the Solaf zone. (b) Close up view showing F_2 isoclinal fold superimposed by F_3 open fold, looking NW. (c) Close up view showing the D_3 sinistral strike–slip movement. (d) Two small-scale domes in the same orientation of the Feiran and the Solaf doubly-plunging antiforms. The small-scale synform (F_4), which separates the two domes, has the orientation of the NE–SW. (e) The migmatites in the core of the Feiran antiform crop out in the more deeply eroded part along Wadi Feiran. (f) Close up view showing the exfoliation appearance of the dolerite plugs at the northeastern part of the Feiran zone (Wadi Rummana). (g) Deformed granitic dyke, the paragneisses around this dyke are rich in K-feldspar. (h) Syn-tectonic granites intruded perpendicular to the metamorphic foliations (S_1) at the end of Wadi Um-Takha.

quartzofeldspathic gneisses. These gneisses lack migmatitic features. There is no contact between the migmatites and the granite intrusions surrounding the FSMC suggesting that the migmatization process is not related to these granites.

The most abundant rock units in the Feiran zone are the hornblende gneiss and the quartzofeldspathic gneiss (Fig. 2). Rare metagraywacke bands occur. There is intercalation and repetition between these two rock types, but the proportion of quartzofeldspathic gneisses increases toward the outer-rim of the Feiran antiform. In the Solaf zone, the quartzofeldspathic gneisses are the predominant rock unit. The hornblende gneiss is fine- to medium-grained, strongly foliated and dark in colour. The quartzofeldspathic gneisses are brownish grey colour, fine- to medium-grained and strongly foliated. The hornblende gneisses consist of hornblende, plagioclase, minor orthoclase and quartz with or without biotite. They also contain subordinate amounts of chlorite, iron oxides, zircon, apatite, titanite and epidote. The quartzofeldspathic gneisses are free of hornblende but otherwise very similar. In the hornblende and the quartzofeldspathic gneisses, the presence of relict sedimentary bedding (e.g. El-Gaby & Ahmed, 1980; El-Gaby *et al.*, 1990; El-Shafei & Kusky, 2003) suggests that they had a sedimentary origin.

The calcsilicates running parallel to and in contact with the granitoid rocks at the outer most rim of the Solaf antiform (Fig. 2) are characterized by well-developed garnet crystals up to several centimetres in size. The matrix is fine-grained, massive and light to dark-green in colour containing calcite, wollastonite, diopside, Ca-amphibole, scapolite, plagioclase and quartz with subordinate amounts of zoisite/clinozoisite.

Minor lithologies (with smaller occurrence than is mappable on Fig. 2) include amphibolites, dolerite plugs and granitic as well as mafic dykes. The amphibolites occur as conformable inter-bedded bands, linear bodies, and irregular lenses in the paragneisses of the Solaf zone and in the syntectonic granitoids. They are composed essentially of hornblende and plagioclase with minor biotite and quartz. Titanite, apatite, epidote and opaques are common accessory minerals. El-Tokhi (1992) suggested an igneous origin for the amphibolites, based on chemical evidence. But, according to Fowler & Hassan (2008) and our field evidence (Fig. 3a), the amphibolites are interpreted to be of sedimentary origin. The dolerites occur as plugs within the hornblende gneisses and the quartzofeldspathic gneisses at the very northeastern part of the Feiran zone (Wadi Rummana) and consist of plagioclase, amphibole, pyroxene relics and iron oxides. The amphibole and the pyroxene occur interstitially between plagioclase crystals. Granitic dykes and pegmatitic veins also cut the region. These are deformed and contain inclusions from the surrounding rocks. The paragneisses around these granitic dykes are enriched in K-feldspar. The amount of K-feldspar in the country rocks increasing toward these dykes (Fig. 3g).

The plutonic rocks in the study area are represented by pre-, syn- and post-tectonic granites and diorite. The pre- and the syn-tectonic granitoid rocks intruded along the southern and eastern borders of the Solaf zone. They extend further east forming numerous low-relief hills characterized by intense shearing and they contain many xenoliths of amphibolite, hornblende gneisses and quartzofeldspathic gneisses (El-Shafei & Kusky, 2003). In the eastern part of the study area, these granites intruded along pre-existing oblique-slip faults and parallel to the metamorphic foliation. In the southern part of the study area, they intruded more or less perpendicular to the metamorphic foliation (Fig. 3h) and along the NE–SW normal faults. The post-tectonic granites are characterized by the absence of the dyke swarms and form large mountainous outcrops bordering the complex along the eastern and the southern parts of the Feiran zone (Gabal El-Banat and Gabal Serbal). A large undeformed diorite body forms an elongated NE-striking intrusion. El-Shafei & Kusky (2003) suggested that this diorite intrusion may have intruded along a pre-existing crustal weakness located between the Solaf and Feiran zones. The entire area is cut by a large number of dyke swarms ranging from the Precambrian to the Cenozoic in age (El-Shafei & Kusky, 2003).

PETROGRAPHY AND MINERAL CHEMISTRY

The rock types of the Feiran–Solaf complex can be grouped into four major types: (i) migmatitic biotite and hornblende gneisses (migmatites); (ii) hornblende gneisses; (iii) quartzofeldspathic gneisses and (iv) calcsilicates. The quartzofeldspathic gneisses have a very simple mineralogy (Fig. 4a) consisting of biotite, quartz, plagioclase and Fe–Ti oxides and will not be discussed further. The calcsilicates have a complicated fluid history and are studied separately (Abu-Alam & Stüwe, Unpublished data). Here, we concentrate on the migmatites, the hornblende gneisses, and the minor but nevertheless important metagraywacke inclusions therein. The minerals were analysed at the Institute of Earth Science, Karl-Franzens-Universität Graz, Austria, using a JEOL JSM-6310 scanning electron microscope following standard procedures, operating in EDS/WDS mode at 5 nA beam current, accelerating voltage 15 kV and duration time is 100 s. The chemical formulae were calculated using the PET1.1 (Dachs, 2004). The mineral abbreviations which will be used in the following sections are from Holland & Powell (1998).

Migmatitic biotite and hornblende gneisses (Migmatites)

The leucosomes are composed of quartz, plagioclase and K-feldspar with or without biotite and the mesosomes contain plagioclase, amphibole, quartz and

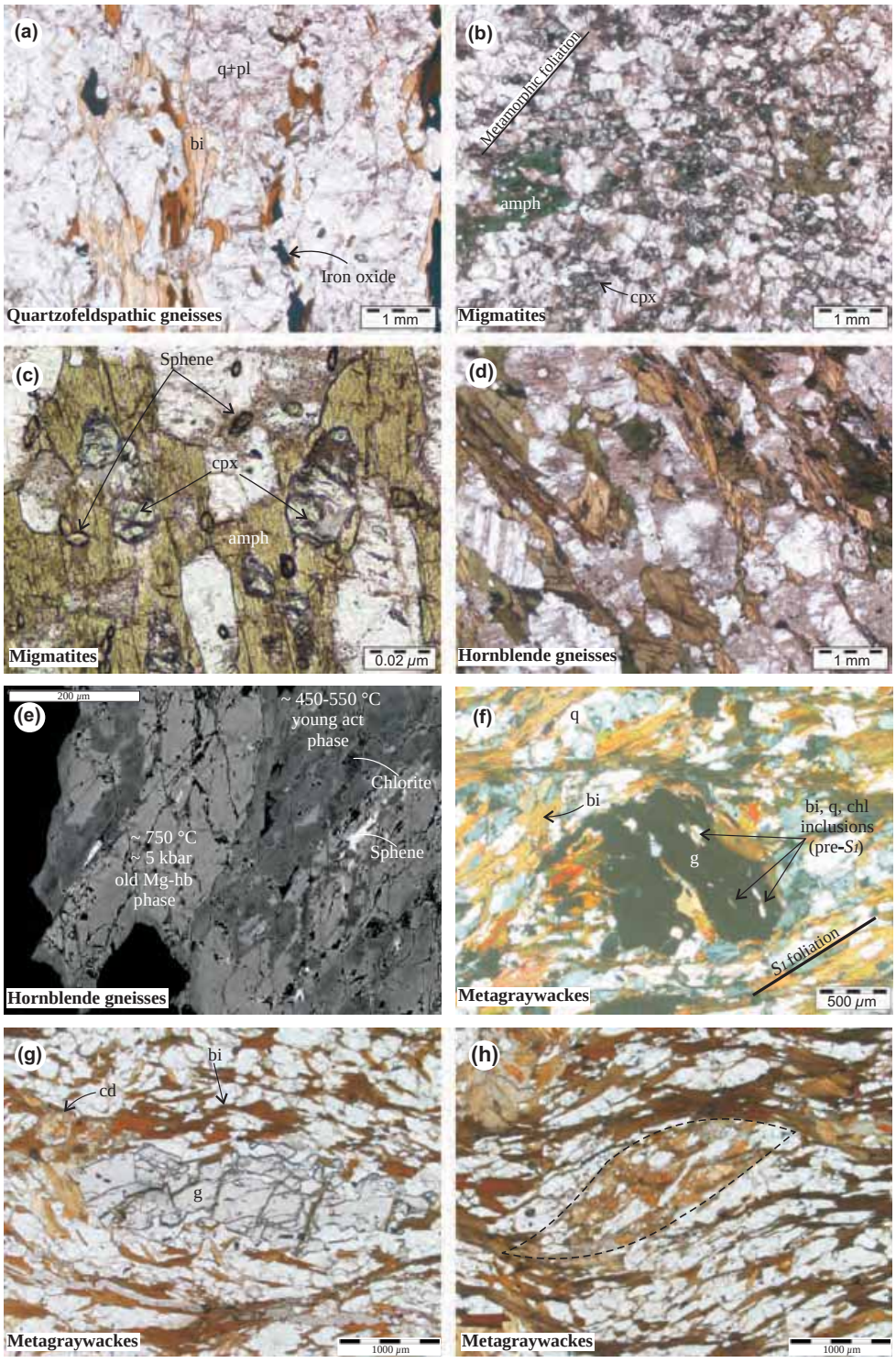

Fig. 4. Photomicrographs of the main rock types. (a) The poor mineral assemblage of the quartzofeldspathic gneisses, (b) Clinopyroxene of sample F39 is highly deformed and aligned along the S_1 foliation. (c) Hornblende porphyroblast of sample F39 has inclusions of clinopyroxene. (d) Metamorphic foliation (parallel crystals of the hornblende) of sample F1. (e) Backscattered-electron image showing two different phases of amphibole, where the high temperature hornblende was replaced by low temperature actinolite. (f) Garnet porphyroblast of sample F93d. This porphyroblast has biotite, plagioclase, quartz and chlorite inclusions. (g) Deformed garnet crystal of sample F93d with long axes parallel to the matrix foliation. (h) Cordierite porphyroblast of sample F93d with sigmoidal shape.

clinopyroxene (in order of abundance) along with minor titanite, magnetite and epidote. Clinopyroxene occurs as anhedral elongated crystals up to 0.3×0.7 mm which are highly deformed and dynamically recrystallized in the S_1 foliation (Fig. 4b). Hornblende occurs as both small grains (< 0.5 mm) and porphyroblasts (> 1.5 mm). The small crystals are highly deformed, parallel to S_1 foliation and in equilibrium with the clinopyroxene. The porphyroblasts are subhedral to anhedral weakly deformed grains. These porphyroblasts have inclusions of clinopyroxene (Fig. 4c). The long axes of the hornblende porphyroblasts are sub-parallel to the S_1 foliation. The hornblende crystals are overgrown by actinolite. Plagioclase occurs as subhedral to anhedral equant crystals attaining $\approx$0.75 mm in diameter and highly altered to epidote. Quartz with undulose extinction occurs interstitially between the plagioclase, hornblende and the clinopyroxene crystals. The magnetite occurs as euhedral crystals (0.3 mm) that overgrow the S_1 foliation. Titanite occurs as small euhedral inclusion crystals (< 0.01 μm) in hornblende porphyroblasts within S_1 foliation (Fig. 4c).

Based on the observations above we interpret the metamorphic peak assemblage as hornblende, clinopyroxene, plagioclase, magnetite and titanite and suggest that it grew during D_1 or just thereafter. The hornblende crystals are overgrown by actinolite and epidote overgrows plagioclase. Therefore, the assemblage hornblende, actinolite, plagioclase, albite, epidote and titanite is interpreted as a later assemblage (post-peak).

The mineral chemistry of the amphibole reveals that they are magnesio-hornblende, edenite, edenitic-hornblende, actinolitic-hornblende and actinolite (Fig. 5a,b). The $X_{Fe}^{hb} = Fe^{+2}/(Fe^{+2} + Mg^{+2})$ ranges (0.385–0.429), while the X_{Fe}^{act} ranges around the value 0.384. The Y(hb) = X(Al, M_2) = (0.121–0.265) and the Y(act) = (0.206–0.207) (Tables 1 & S1). The cores of the plagioclase (pre-peak assemblage) have X(an) = Ca/(Ca + Na + K) ranges between 0.297 and 0.30, the plagioclase of the peak assemblage has X(an) = (0.278–0.281), while plagioclase associated with the late epidote and actinolite (post-peak assemblage), has X(an) = (0.252–0.278) (Table S2). Clinopyroxene has diopside–augite composition (Fig. 5c) with $X_{Fe} = Fe^{+2}/(Fe^{+2} + Mg^{+2})$ = (0.401–0.431) (Tables 1 & S3).

Hornblende gneisses

The mineralogy of the hornblende gneisses includes hornblende, actinolite, plagioclase, albite, K-feldspar, quartz, chlorite as well as accessory amounts of epidote, magnetite, ilmenite, titanite, apatite and zircon. Plagioclase and amphibole are the most abundant minerals, amounting to $\sim$80 vol.%. Plagioclase occurs as anhedral to subhedral elongated crystals attaining 0.35×0.7 mm. The plagioclase crystals show albite and albite-Carlsbad twinning, but untwined crystals are observed too. The plagioclase crystals are highly retrogressed to epidote. Hornblende is a green colour and strongly pleochroic. Hornblende occurs as anhedral elongated crystals (1.63×0.68 mm) (Fig. 4d). Hornblende is retrogressed to actinolite, chlorite and titanite (Fig. 4e). Quartz occurs as anhedral to subhedral crystals that lie interstitially between the plagioclase and the hornblende crystals. It frequently exhibits undulose extinction. The long axes of the plagioclase and the hornblende crystals are parallel to the metamorphic foliation (Fig. 4d). K-feldspar occurs as very small (apparent only under the scanning electron microscope) anhedral equant crystals, which lie interstitially between the plagioclase, the quartz and the hornblende crystals. Ilmenite grows over magnetite as lamellar intergrowths.

The peak assemblage is identified by a continuous metamorphic foliation, which is defined by parallel crystals of hornblende, plagioclase, quartz and iron oxides (Fig. 4d). The retrogression of plagioclase to epidote and hornblende to actinolite, chlorite and titanite as well as the presence of albite identify the retrograde assemblage. The large difference between the crystal size of the K-feldspar and the surrounding minerals, the anhedral shape of the K-feldspar crystals as well as the presence of K-feldspar-rich metasomatic zones around the granitic dykes (Fig. 3g) suggests that the K-feldspar are in disequilibrium with the other phases.

Chemical analyses reveal that the studied amphiboles are magnesio-hornblende, edenite, actinolitic-hornblende and actinolite (Fig. 5a,b). The Al_2O_3 value ranges between 8.11 and 7.79 wt.% for the magnesio-hornblende and the edenite, while this value ranges between 2.69 and 4.34 wt.% for the actinolitic-hornblende and the actinolite (Tables 1 & S4). The X_{Fe}^{hb} ranges (0.475–0.477), while the X_{Fe}^{act} ranges (0.214–0.226). The Y(hb) = (0.063–0.066) and the Y(act) = (0.16–0.22). The decrease in the Al^{IV} and Al^{VI} from earlier to later amphiboles (from hornblende to actinolite) reveals that the amphibole goes from relatively high temperature–high pressure field to low temperature–low pressure field (Rasse, 1974; Blundy & Holland, 1990) (Fig. 5d). The relationship between Al^{VI} and Si (Fig. 5e) indicates that the hornblende crystallized under pressure of $\leq$5 kbar while the pressure of the actinolite is most probably < 5 kbar (Fig. 5d). According to the graphical geothermometer of Blundy & Holland (1990), the hornblende crystallized at a temperature below $\sim$750 °C, while actinolite formed between 450–600 °C (Fig. 5f).

Metagraywackes

In Wadi Aleiyat (Fig. 2) a few rock bands were found that contain cordierite and garnet. These rocks have a metagraywacke bulk composition similar to sample ES356 of Sawyer (1986) which was modelled by

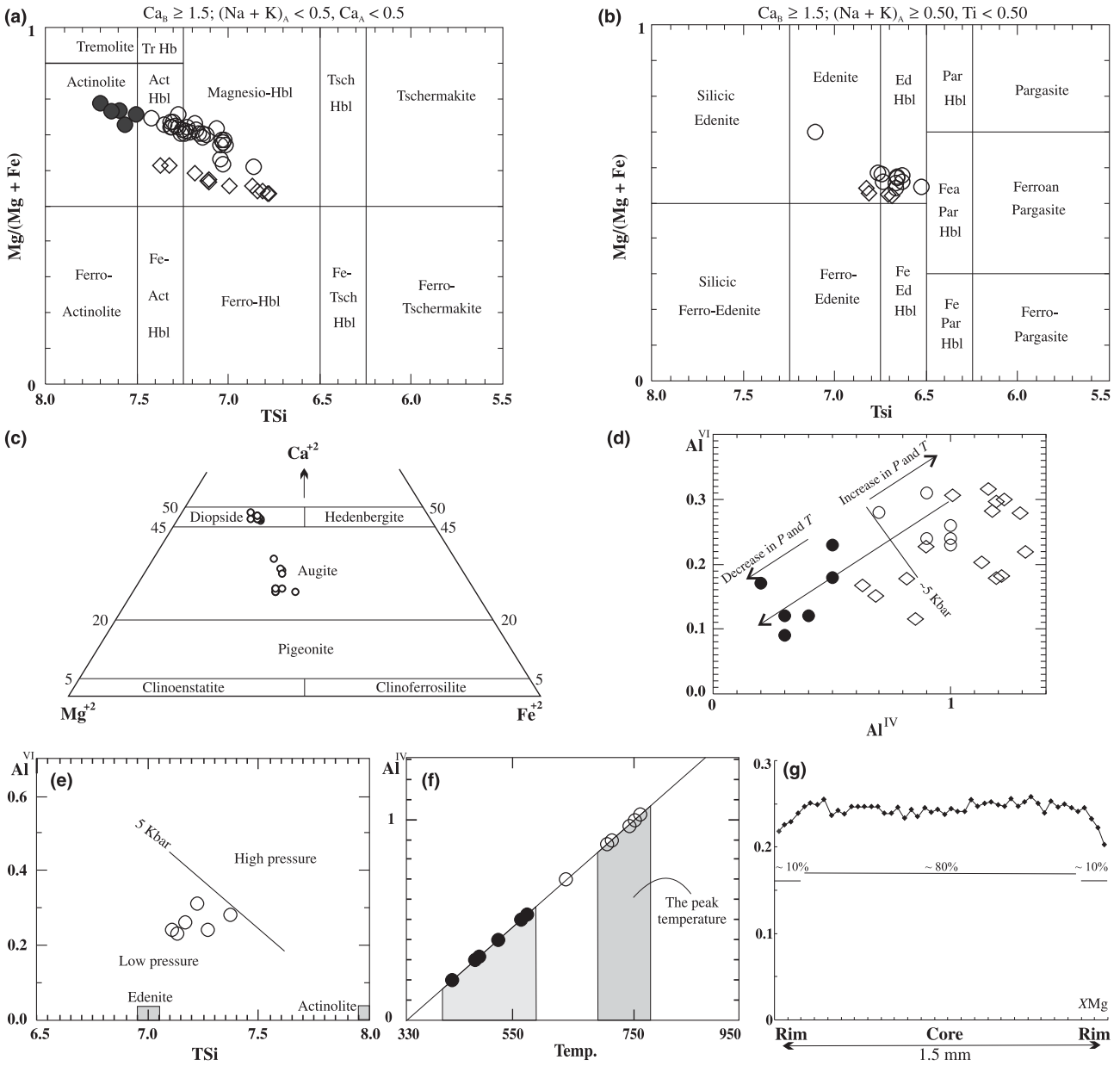

Fig. 5. Amphibole chemistry. (a) and (b) Amphibole composition classified after Leake *et al*. (1997). (c) Ca–Mg–Fe composition ranges and nomenclature of clinopyroxene (after Morimoto, 1988). (d) Shows the relation between the Al^{IV} and Al^{VI} in the amphibole of samples F1 and F63. (e) Relation between Al^{VI} and Si of hornblende (after Rasse, 1974). (f) Al^{IV} *v*. temperature for amphiboles after Blundy & Holland (1990). The open circle is the hornblende of the hornblende gneisses (the old phase), the filled circle is actinolite of the hornblende gneisses (the young phase) and the rhomb is the amphibole of the migmatite. (g) Zoning profile of $X\mathrm{Mg} = Mg^{+2}/(Fe^{+2} + Mg^{+2} + Mn^{+2})$ through garnet grain.

Johnson *et al*. (2008, e.g. their fig. 3a). Because these rocks prove to be petrologically useful (see below), they are described in detail here although they are quite rare in the FSMC. The rocks contain biotite, garnet, cordierite, plagioclase, quartz, chlorite, ilmenite and rutile. Muscovite and K-feldspar are notably absent. Garnet and cordierite occur as porphyroblasts (Fig. 4f). Garnet porphyroblasts are subhedral to anhedral equant grains up to 5 mm in diameter with inclusions of quartz, plagioclase, biotite, chlorite and ilmenite. The inclusions define linear trails that are oblique to the matrix foliation (S_1) giving relic evidence to an earlier deformation phase prior to D_1. Some garnet is idiomorphic and has straight crystal boundaries against biotite in the matrix. Other garnet crystals are highly deformed with long axes parallel to the matrix foliation (Fig. 4g). The cordierite porphyroblasts are anhedral, highly altered grains 0.5 mm and 3 mm in diameter. The cordierite crystals are equidimensional porphyroblasts with sigmoidal shape

Table 1. Representative mineral analyses of samples F39, F1 and F63; amphibole (normalized to 23 O and ignoring H_2O), plagioclase (normalized to 8 O) and pyroxene (normalized to 6 O).

Sample no.	F39														F1		F63	
Assemblage	hb di pl mt sph (peak assemblage)				hb di pl sph (pre-peak ass.)					hb act pl ep sph (post-peak ass.)			hb act ab ep sph (late post-peak ass.)					
Mineral	hb6	hb14	pl28	pl31	hb13	pl16	pl18	py2	py30	act2	pl3	pl15	ab3	ab8	hb3	act2	hb8	act3
SiO_2	47.28	48.78	61.35	61.61	44.89	60.9	61.04	50.06	48.4	49.44	61.96	61.65	68.59	69.03	42.56	54.09	42.72	52.35
TiO_2	0.58	0.47	0.03	b.d.l.	0.94	0.05	b.d.l.	0.12	0.96	0.57	b.d.l.	0.03	b.d.l.	b.d.l	0.92	0.13	0.98	0.23
Al_2O_3	6.07	6.18	23.84	23.98	8.95	24.56	24.48	5.37	7.49	5.05	24.03	23.73	19.55	19.57	9.1	2.69	8.58	4.34
Cr_2O_3	0.02	0.01	b.d.l.	b.d.l.	0.05	0.03	b.d.l.	0.02	b.d.l.	b.d.l.	b.d.l.	0.03	0.02	b.d.l	b.d.l	0.09	b.d.l.	0.06
FeO	16.85	16.1	0.27	0.15	18.45	0.29	0.26	14.54	16.81	15.27	0.24	0.42	b.d.l	b.d.l	20.22	8.89	18.43	9.49
MnO	0.62	0.64	0.1	b.d.l	0.58	b.d.l	0.03	0.73	0.63	0.56	0.04	b.d.l.	b.d.l	b.d.l	0.69	0.56	0.45	0.49
MgO	12.66	13	0.04	b.d.l.	11.31	b.d.l.	b.d.l.	12.18	11.66	13.5	b.d.l.	b.d.l.	0.02	b.d.l	9.89	18.26	11.33	17.81
CaO	11.34	11.65	5.9	5.82	11.51	6.14	6.11	15.82	11.52	11.37	5.15	5.74	0.4	0.3	11.74	11.69	12.52	11.37
Na_2O	0.87	0.81	8.13	8.18	1.17	7.8	7.86	0.65	1.19	0.75	8.00	8.03	11.22	11.38	1.64	0.39	1.4	0.57
K_2O	0.61	0.54	0.32	0.24	0.98	0.19	0.19	0.07	0.82	0.62	0.68	0.32	0.01	0.01	0.89	0.17	0.8	0.22
Total	96.94	98.22	99.97	99.98	98.87	99.96	99.96	99.56	99.48	96.98	100.12	99.95	99.8	100.29	97.65	96.96	97.21	96.93
O	23	23	8	8	23	8	8	6	6	23	8	8	8	8	23	23	23	23
Si	7.05	7.15	2.73	2.73	6.64	2.7	2.71	1.74	1.83	7.32	2.74	2.74	2.99	3.00	6.44	7.71	6.52	7.49
Ti	0.06	0.05	0.00	–	0.1	0.00	–	0.31	0.02	0.06	–	0.00	–	–	0.14	0.01	0.15	0.02
Al	1.06	1.06	1.25	1.25	1.56	1.28	1.28	0.22	0.33	0.88	1.25	1.24	1.01	1.00	1.62	0.45	1.54	0.73
Cr	0.00	0.00	–	–	0.01	0.00	–	0.00	–	–	–	0.00	0.00	–	–	0.01	–	0.01
Fe^{+3}	0.32	0.18	0.01	0.01	0.4	0.01	0.01	0.00	0.00	0.02	0.01	0.01	–	–	0.53	0.00	0.00	0.02
Fe^{+2}	1.77	1.78	0.00	0.00	1.87	0.00	0.00	0.42	0.51	1.86	0.00	0.00	–	–	2.03	1.06	2.35	1.11
Mn	0.07	0.08	0.00	–	0.07	–	0.00	0.02	0.02	0.07	0.00	–	–	–	0.09	0.06	0.06	0.05
Mg	2.81	2.84	0.00	–	2.49	–	–	0.63	0.67	2.98	–	–	0.00	–	2.23	3.88	2.58	3.8
Ca	1.81	1.83	0.28	0.27	1.82	0.29	0.29	0.59	0.46	1.8	0.24	0.27	0.02	0.01	1.90	1.78	2.05	1.74
Na	0.25	0.23	0.7	0.7	0.33	0.67	0.67	0.04	0.08	0.21	0.68	0.69	0.95	0.96	0.48	0.1	0.41	0.15
K	0.11	0.1	0.02	0.01	0.18	0.01	0.01	0.00	0.04	0.11	0.04	0.02	0.00	0.00	0.17	0.03	0.16	0.04
X_{Fe}^{hb} or ^{act}	0.387	0.385			0.429					0.384					0.475	0.214	0.477	0.226
Y(hb) or (act)	0.121	0.221			0.207					0.207					0.063	0.16	0.066	0.22
X(an)			0.281	0.278		0.300	0.297				0.252	0.278	0.020	0.010				
X_{Fe}^{di}								0.401	0.431									

Additional data are in the online data repository.

in S_1 (Fig. 4h). Cordierite porphyroblasts have quartz, plagioclase, biotite, chlorite and ilmenite inclusions. Garnet and cordierite porphyroblasts are surrounded by a matrix of biotite, plagioclase, chlorite, quartz, ilmenite and rutile that define a continuous S_1 foliation. The plagioclase occurs as euhedral to anhedral elongate crystals attaining 0.15×0.3 mm. Quartz occurs as anhedral to subhedral crystals that lie interstitially between the plagioclase and the biotite crystals. Biotite occurs as anhedral to subhedral flaky and stumpy crystals attaining $\sim 0.25 \times 0.75$ mm and is rarely overgrown by chlorite.

Garnet is weakly zoned (Fig. 5g). The cores of these garnet crystals have Mg contents between 0.71 and 0.75 and Fe^{+2} contents between 1.91 and 1.92, with $X_{Fe}^{g} = Fe^{+2}/(Fe^{+2} + Mg^{+2}) = (0.72–0.73)$ and $Z(g) = Ca/(Fe + Mg + Ca) = (0.04–0.044)$. The rims of these garnet crystals have Mg cation range between 0.61 and 0.69 and Fe^{+2} cation range between 1.83 and 1.9, with $X_{Fe}^{g} = (0.734–0.752)$ and $Z(g) = (0.04–0.048)$. The cordierite is Mg-rich, with Mg and Fe^{+2} cations (1.37–1.49) and (0.49–0.53) respectively. The $X_{Fe}^{cd} = Fe^{+2}/(Fe^{+2} + Mg^{+2})$ ranges (0.250–0.261). The biotite within the matrix (S_1 biotite), has $X_{Fe}^{bi} = Fe^{+2}/(Fe^{+2} + Mg^{+2})$ ranges (0.468–0.483) and $Y(bi) = X(Al, M_2) = (0.27–0.29)$ (Table S5). The chlorite minerals have $X_{Fe}^{chl} = Fe^{+2}/(Fe^{+2} + Mg^{+2}) = (0.381–0.4)$ Table S6.

Biotite–plagioclase–garnet geothermometery of Bhattacharya *et al.* (1992) gives a temperature of 668–707 °C for the peak assemblage and 676–722 °C using the thermometer of Ganguly & Saxena (1984). The same minerals gave a pressure range of 6.2–8 kbar according to Hoisch (1990) (Tables 2 & S7). The cordierite–garnet (garnet-rim) geothermometer according to Thompson (1976) gave a temperature range between 654 and 649 °C and a range between 635 and 638 °C according to Perchuk & Lavrent'eva (1983) Table S8.

The presence of highly deformed garnet crystals which have long axes parallel to the matrix foliation S_1 indicates that it grew early during D_1. The sigmoidal shapes of the cordierite crystals indicate that these porphyroblasts grew later – possibly during D_2. The peak assemblage was identified by the presence of garnet porphyroblasts. Based on these observations, the peak metamorphism was interpreted as an event between D_1 and D_2. Biotite, chlorite, plagioclase, quartz and ilmenite inclusions inside the garnet porphyroblasts were interpreted as the pre-peak assemblage while biotite, chlorite, plagioclase, quartz, ilmenite, rutile (matrix mineral) with or without cordierite were interpreted as the post-peak assemblage. The presence of idiomorphic garnet crystals (Vernon, 2004) as well as the temperatures given by the biotite–plagioclase–garnet geothermometer possibly indicates that the rocks reached peak conditions above the

Table 2. Representative mineral analyses and conventional thermobarometers of sample F93d; biotite (normalized to 11 O and ignoring H_2O), chlorite (normalized to 14 O and ignoring H_2O), cordierite (normalized to 18 O and ignoring H_2O), plagioclase (normalized to 8 O) and garnet (normalized to 12 O).

Assemblage	bi chl pl ru ilm H_2O (latest post–assemblage)						bi g pl ilm H_2O (peak assemblage)						bi cd pl ilm H_2O (post–peak assemblage)			
Mineral	bi11	bi20	chl4	chl5	chl31	chl33	g16	bi18	pl4	g17	bi17	pl5	cd3	cd8	bi3	bi13
SiO_2	35.33	25.20	25.76	25.34	28.13	27.93	37.37	35.46	59.93	38.05	36.02	63.68	48.91	47.47	34.63	34.13
TiO_2	1.78	2.14	0.38	0.38	0.12	0.26	0.17	2.49	b.d.l	0.07	1.61	0.09	b.d.l	b.d.l	2.94	1.77
Al_2O_3	18.39	19.27	21.45	21.50	19.85	18.43	20.42	18.85	23.13	20.69	19.69	21.19	32.59	32.21	18.5	18.67
Cr_2O_3	0.07	0.17	0.10	0.10	0.01	0.12	0.02	0.07	0.06	0.08	0.17	b.d.l	b.d.l	0.07	0.26	0.04
FeO	19.20	18.64	20.35	20.17	21.96	21.92	30.07	19.36	0.94	30.08	19.20	0.59	5.79	5.92	18.12	19.19
MnO	0.16	0.16	0.11	0.11	0.23	0.23	3.14	0.13	0.03	3.32	0.16	0.05	0.29	0.11	0.22	0.48
MgO	12.21	11.18	17.99	17.83	18.60	18.54	6.29	10.32	1.66	6.08	10.68	0.46	9.7	9.38	11.41	12.21
CaO	0.12	b.d.l	b.d.l	b.d.l	0.01	0.09	1.30	0.12	4.42	1.43	0.13	7.7	0.06	0.04	0.13	0.16
Na_2O	0.41	0.42	b.d.l	b.d.l	b.d.l	b.d.l	b.d.l	0.41	9.17	b.d.l	0.42	7.20	b.d.l	b.d.l	0.41	0.44
K_2O	8.71	9.90	0.05	0.04	0.07	0.15	0.05	9.55	0.12	b.d.l	8.57	0.18	0.03	b.d.l	9.12	7.97
O	11	11	14	14	14	14	12	11	8	12	11	8	18	18	11	11
Si	2.64	2.62	2.68	2.66	2.85	2.88	2.95	2.65	2.66	2.98	2.67	2.78	5.03	4.99	2.62	2.60
Ti	0.1	0.12	0.03	0.03	0.01	0.02	0.01	0.14	–	0.00	0.09	0.00	–	–	0.16	0.10
Al	1.62	1.69	2.63	2.66	2.37	2.24	1.9	1.66	1.21	1.91	1.72	1.09	3.95	3.99	1.65	1.67
Cr	0.00	0.01	0.01	0.01	0.00	0.01	0.00	0.00	0.00	0.01	0.01	–	–	0.01	0.01	0.002
Fe^{+3}	0.00	0.00	0.00	0.00	0.00	0.00	0.13	0.00	0.07	0.1	0.00	0.04	0.00	0.00	0.00	0.00
Fe^{+2}	1.2	1.16	1.77	1.77	1.86	1.89	1.9	1.21	0.00	1.9	1.19	0.00	0.49	0.52	1.14	1.22
Mn	0.01	0.01	0.01	0.01	0.02	0.02	0.21	0.01	0.00	0.22	0.01	0.00	0.03	0.01	0.01	0.03
Mg	1.36	1.24	2.79	2.79	2.81	2.85	0.75	1.15	0.11	0.73	1.18	0.03	1.49	1.47	1.28	1.38
Ca	0.01	–	–	–	0.00	0.01	0.11	0.01	0.21	0.12	0.01	0.36	0.01	0.01	0.01	0.01
Na	0.06	0.06	–	–	–	–	–	0.06	0.79	–	0.06	0.61	–	–	0.06	0.06
K	0.83	0.94	0.01	0.01	0.01	0.02	0.01	0.91	0.01	–	0.81	0.01	0.00	–	0.88	0.77
X_{Fe}^{bi}	0.467	0.483													0.471	0.468
X_{Fe}^{chl}			0.388	0.388	0.397	0.399										
X_{Fe}^{g}							0.711			0.722						
Z(g)							0.040			0.044						
Y(bi)	0.26	0.31						0.31			0.39				0.27	0.29
P kbar (Hoisch, 1990)								8.1			6.2					
T °C (Bhattacharya *et al.*, 1992)								706			675					
T °C (Ganguly & Saxena, 1984)								723			697					

solidus. However, as the metagraywackes do not have any partial melting indications in the field, we suggest that the liquid mode in the rock during the peak conditions was below 5% (Sawyer, 1999).

PSEUDOSECTIONS

Pseudosections were constructed for several bulk compositions to constrain the P, T and Xo paths. Four samples were chosen to represent the rock types discussed above. Sample F39 was chosen to represent the migmatites. It is from one of the pyroxene-bearing mesosomes in the central part of the study area (28°42′13″N and 33°39′30″E; Fig. 2). Samples F1 and F63 are hornblende gneisses from the next higher unit. They were collected at 28°44′28″N and 33°34′44″E (F1) and at 28°43′39″N and 33°32′41″E (F63). Sample F93d is characterized by the presence of garnet and cordierite porphyroblasts. This sample was collected from one of the rare metagraywacke bands which are intercalated with the hornblende gneisses and the quartzofeldspathic gneisses at the end of Wadi Aleiyat (28°40′52″N and 33°39′37″E; Fig. 2).

For bulk rock chemical analysis a Bruker Pioneer S4 X-ray fluorescence spectrometer was used at the Institute of Earth Science, Karl-Franzens-Universität, Graz, Austria. Samples were prepared as fused pellets using $Li_2B_4O_7$ flux. The pseudosections were constructed using THERMOCALC tc330 (Powell & Holland, 1988) and the internally consistent dataset of Holland & Powell (1998). The following a–x models were used: amphibole (Diener *et al.*, 2007); muscovite/paragonite (Coggon & Holland, 2002); biotite (White *et al.*, 2007); orthopyroxene (White *et al.*, 2002); clinopyroxene (Green *et al.*, 2007); plagioclase/K-feldspar (Holland & Powell, 2003); garnet (White *et al.*, 2007); cordierite (Holland & Powell, 1998); chlorite (Mahar *et al.*, 1997; Holland *et al.*, 1998); epidote (Holland & Powell, 1998); melt (White *et al.*, 2007); ilmenite/hematite (White *et al.*, 2000) and magnetite/spinel (White *et al.*, 2002).

Migmatites *P–T* pseudosection

The XRF whole-rock analysis of sample F39 showed that the K_2O and the MnO constitute $<1\%$ of the bulk rock (Table 3). Therefore, the P–T pseudosection for this sample was calculated in the system NCFMASHTO for the phases listed in the figure caption of Fig. 6a and for quartz in excess. As there is no melt model for this system, it is only meaningful to interpret the sub-solidus parts of the P–T path for this sample where water is likely to have been present.

Table 3. Representative XRF analyses of different rock groups; major elements in wt%, trace elements (ppm).

Group	Sample	LOI	SiO_2	Al_2O_3	$Fe_2O_3^{tot}$	MnO	MgO	CaO	Na_2O	K_2O	TiO_2	P_2O_5	Sum	Ba	Ce	Cr	Rb	Sr)	V	Y	Zn	Zr
Hornblende gneisses	F59	1.39	67.16	15.47	4.45	0.08	1.84	3.25	4.46	1.43	0.71	0.22	100.60	354	33	< 20	39	483	86	22	86	160
	F1	0.87	64.67	14.43	6.21	0.13	2.96	3.44	4.93	0.95	0.85	0.21	99.81	465	42	97	38	332	128	27	94	171
	F63f	1.20	61.81	16.78	6.54	0.11	2.13	4.50	5.34	0.93	0.95	0.31	100.73	188	77	< 20	< 15	526	129	39	66	208
	F4	0.54	62.47	15.34	6.68	0.15	3.07	5.00	4.96	0.94	0.97	0.22	100.47	253	54	105	< 15	370	146	34	86	182
	F7	0.27	66.93	15.11	6.57	0.07	1.80	2.40	4.71	1.70	0.89	0.17	100.81	679	57	61	39	377	116	32	59	227
Quartzofeldspathic gneisses	F77	0.56	77.58	12.10	1.22	0.06	0.47	1.39	1.52	5.73	0.13	b.d.l	100.93	839	27	< 20	195	31	< 20	< 20	48	108
	F77a	0.65	81.62	10.21	1.12	0.13	0.43	2.20	2.30	1.77	0.11	b.d.l	100.67	720	33	< 20	61	34	< 20	24	24	103
	F35	0.58	64.37	13.39	3.69	0.67	2.17	7.79	2.63	4.75	0.49	0.20	100.92	773	68	22	138	140	31	32	377	252
Calcsilicate	F51b	13.18	40.59	4.20	0.93	0.22	1.36	37.23	1.26	0.64	0.17	0.07	99.90	115	< 30	25	< 15	371	50	< 20	26	49
	F33	1.33	53.83	9.91	4.09	0.28	2.07	23.87	2.63	1.92	0.40	0.16	100.58	349	43	30	42	133	66	26	205	108
Migmatite	F39	0.75	59.91	14.59	6.20	0.24	4.08	8.13	4.21	0.73	0.78	0.21	99.96	167	60	96	< 15	409	118	38	91	166
Metagraywackes	F93d	1.57	60.82	14.60	8.91	0.11	5.00	2.01	2.34	3.15	0.97	0.15	99.83	483	84	429	90	162	143	25	96	202
	F93a	1.00	46.95	2.17	34.93	0.07	2.21	7.44	b.d.l	b.d.l	0.15	5.17	100.22	24	< 30	26	< 15	544	36	< 20	61	88
	F93c	1.00	47.72	4.26	27.53	0.09	2.31	10.05	0.25	b.d.l	0.22	6.83	100.41	83	< 30	37	< 15	574	43	< 20	53	170
	F94a	1.50	55.26	20.64	6.25	0.10	2.68	7.79	3.03	1.54	0.87	0.22	100.05	433	22	31	64	661	137	28	75	134

Thus, for Fig. 6a, water was chosen to be in excess. As a reference for the onset of melting, we have superimposed the initial melting reactions in the system NCKFMASHTO on Fig. 6a keeping in mind that all equilibria at temperatures above this line must be interpreted with care (as the water saturated assumption does not hold there).

The *P–T* pseudosection for sample F39 is characterized by a series of mineral assemblage fields with steep boundaries (Fig. 6a). Only one small divariant field (hb + act + di + pl + ab + ep + sph) appears at 7.4–8.3 kbar and 520–535 °C. The hb + di + pl + sph pentivariant field is the largest field and is stable at 4.3–10 kbar and 525–795 °C. Magnetite-in reactions appear between 3 kbar – 485 °C and 9 kbar – 800 °C. The proportion of magnetite increases with increasing temperature. The amphibolite to granulite facies boundary identified by the first appearance of orthopyroxene, occurs at ~760 °C. The melting reactions appear as near isothermal reactions between (625 °C – 10 kbar) and (675 °C – 3 kbar). The stability fields of albite appear at low temperature conditions (430 °C – 3 kbar) while this temperature increases with the increase of pressure (560 °C – 10 kbar).

The migmatite peak assemblage of hb + di + pl + mt + sph appears on Fig. 6a in a quadrivariant field in the region (580–760 °C at 3 kbar), and narrows to higher pressure where it terminates at 785 °C at 8.65 kbar. Within this field, the peak conditions can be further constrained using the X_{Fe}^{hb} and the *Y*(hb) isopleths. However, much of this field is within the partial melting region for which Fig. 6a is not well constrained. Thus, while isopleths indicate peak conditions between 5.3 and 7.8 kbar we suggest that these cannot be used for further interpretation. A lower limit of the temperature at the metamorphic peak is identified as the first appearance of the melt at 660 °C while an upper temperature limit is identified by the absence of orthopyroxene, which appears above 775 °C.

Conditions for the pre-peak assemblage hb + di + pl + sph are mainly defined on the basis of the different chemistry of texturally earlier amphibole and plagioclase crystals. The estimated temperature for these minerals is 555–655 °C. Unfortunately, because of the parallelism of the mineral isopleths (Fig. 6a), there are no pressure constraints. The post-peak conditions are well preserved by the presence of the hb + act + pl + ep + sph assemblage. The hb + act + pl + ep + sph assemblage was contoured for the X_{Fe}^{act} and the *X*(an) isopleths (Table 1), to constrain the retrograde pressure and the temperature conditions. The isopleths reveal that this mineral assemblage was stable at temperature range of (455–520 °C). Because of the presence of the albite, the migmatites were re-equilibrated at low temperature (< 450 °C). The pressure range at the low temperature condition cannot be closely constrained, but the actinolite chemistry (Fig. 5d) is consistent with cooling most probably < 5 kbar.

Hornblende gneiss *P–T* pseudosections

The *P–T* pseudosection for the hornblende gneisses (samples F1 & F63) was calculated in the system NCFMASHTO (Fig. 6b) for a bulk composition from XRF neglecting 0.95 wt% K_2O (Table 3). Calculations were performed assuming water to be in excess which is likely to be justified in the light of the fact that these rocks show no evidence for partial melting.

The *P–T* pseudosection is characterized by a series of mineral assemblage fields with steep boundaries, except the garnet-in reactions (Fig. 6b). The garnet-bearing assemblages appear at high temperature and high pressure conditions (> 600 °C and > 8.8 kbar). Only one and small isothermal divariant field (hb + chl + pl + ab + ep + sph + ilm) occurs at 3–8 kbar and 457–520 °C. All the assemblages below 565 °C – 3 kbar and 620 °C – 10 kbar are free of magnetite. The first appearance of magnetite is in the trivariant hb + chl + pl + g + ilm + mt and in the quadrivariant hb + chl + pl + ilm + mt fields. The largest field in the *P–T* pseudosection is the pentivariant field hb + pl + ilm + mt. This assemblage is stable at the range of 572–755 °C at 3 kbar, 625 °C – 8.8 kbar and 791 °C – 9.65 kbar. The albite-bearing assemblages appear at low temperature conditions 460 °C – 3 kbar and 550 °C – 10 kbar.

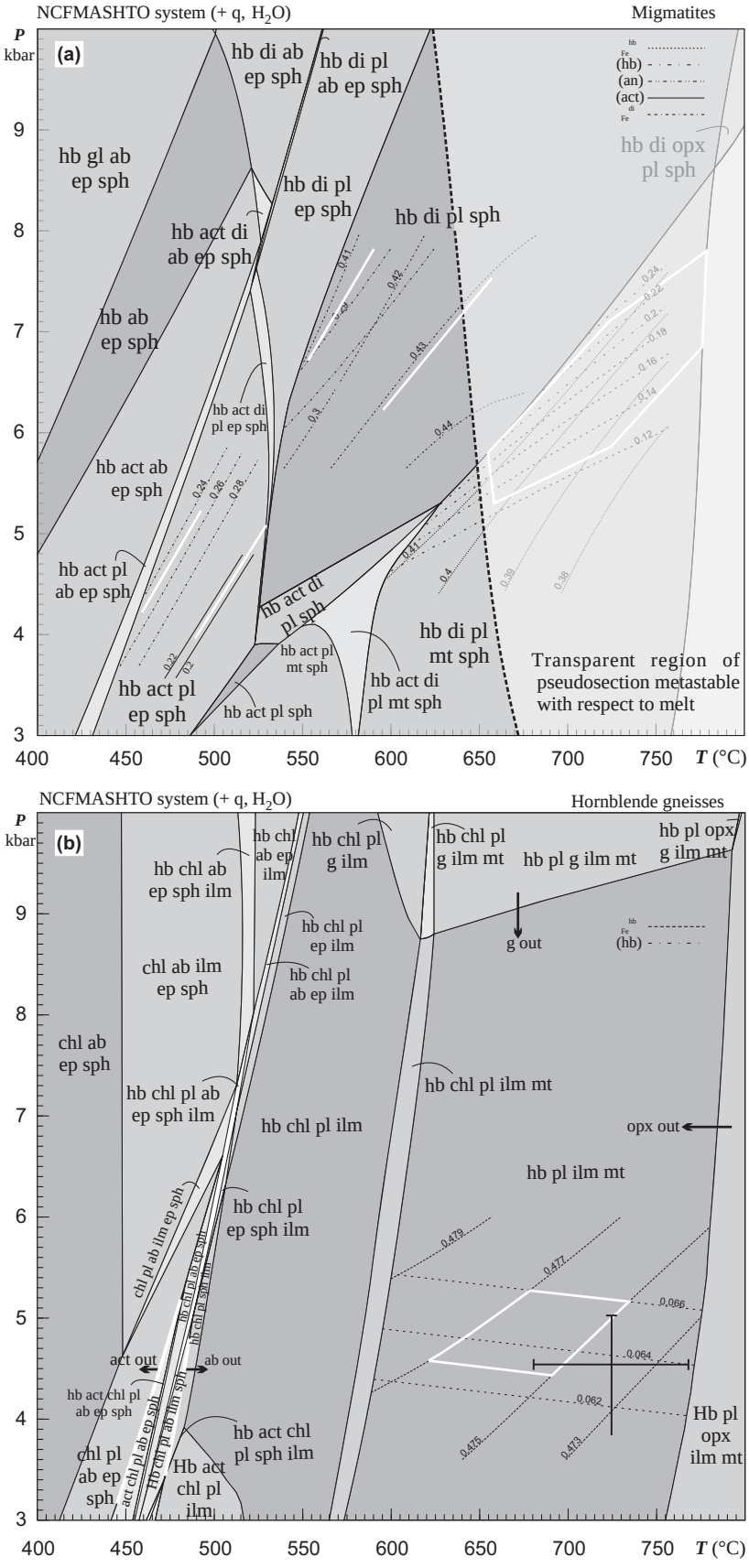

Fig. 6. *P–T* pseudosections for migmatites and hornblende gneisses. For both rock types, the oxidation state was calculated using Le Maitre (1976) equation for the partitioning of FeO and Fe_2O_3 from $Fe_2O_3^{tot}$. (a) *P–T* pseudosection of migmatite sample F39. The bulk composition is (mol.%): SiO_2: 64.12, Al_2O_3: 9.20, CaO: 9.38, MgO: 6.55, FeO: 5.41, Na_2O: 4.38, TiO_2: 0.63, O: 0.32. The thick dashed line shows the first appearance of the melt and was calculated in the system NCKFMASHTO using K_2O: 0.73%. As this line was not calculated in the system for which the pseudosection is drawn, the region above it cannot be interpreted (shaded region). (b) *P–T* pseudosection of average composition of samples F1 and F63. The bulk composition is (mol. %) SiO_2: 69.56, Al_2O_3: 9.98, CaO: 4.36, MgO: 4.22, FeO: 5.34, Na_2O: 5.53, TiO_2: 0.75, O: 0.27. The vertical and the horizontal bars are the average *P* and *T* according to Fig. 5. The white polygons indicate conditions constrained by mineral isopleths.

The absence of orthopyroxene and garnet in the peak assemblage hb + pl + ilm + mt constrains the peak conditions to below 760 °C and 9 kbar. X_{Fe}^{hb} and Y(hb) contours (Table 1) were added to the peak assemblage field in order to constrain the P–T conditions of the equilibrium assemblage in more detail. These conditions are agreement with the metamorphic conditions derived from the relationship between Al^{VI} and the Si and the graphical geothermometer (Fig. 5e,f). The post-peak conditions are difficult to determine. Some constraints however are provided by the late stage minerals chlorite, albite, actinolite and epidote. The presence of these phases implies that the hornblende gneisses re-equilibrated below the albite-in boundary and above the actinolite-out boundary (465–480 °C and $<<5$ kbar according to Fig. 4d,e).

Metagraywacke *P–T* pseudosection

In contrast to the migmatites and the hornblende gneisses, the metagraywackes contain a series of Fe-bearing phases (garnet, cordierite and biotite). For the metagraywackes, we did not rely on Le Maitre (1976) equation to constrain the oxidation state, but constrained it in more detail using a T–Xo pseudosection. Indeed, the mineralogy of this sample does allow a much closer constraint using this method than the mineralogy of the other rock types would. A T–Xo pseudosection (Fig. 7a) of the metagraywackes (sample F93d) was constructed in the system NCKFMASHTO at 8 kbar (the pressure given by biotite–plagioclase–garnet equilibria, Table 2). The loss of ignition (LOI = 1.57) was used to evaluate the H_2O content of this sample. Z(g) isopleths and liquid modes were added to the peak assemblage bi + g + pl + ilm + liq in order to constrain the correct T–Xo conditions. The Z(g) isopleths (0.04–0.044) intersected with 0.05 liquid mode below 735 °C and in a range of Xo of 0.09–0.17. From the T–Xo pseudosection, the best Xo estimate is 0.13, which is equivalent to an oxidation state with a free oxygen content of 0.43.

Using this bulk composition, a P–T pseudosection of the metagraywackes was constructed in the system NCKFMASHTO. This pseudosection shows that gedrite is stable over a wide P–T range – which is not observed in the metagraywackes of the FSMC. We suggest that this can be explained through a fractionation in bulk composition during the retrograde path (Stüwe, 1997): garnet crystals are only zoned along ~20% of their margins (Fig. 5g) indicating that most of their volume was effectively removed from the bulk composition at the peak. We have therefore used the bulk composition described above only to interpret the peak conditions (Fig. 7b). For the interpretation of the retrograde evolution a new effective bulk composition was calculated by removing 80% of the garnet from the bulk of Fig. 7b (Fig. 7c).

Both pseudosections (Fig. 7b,c) are characterized by the absence of univariant and divariant assemblages. There is one trivariant field; the bi + hl + pl + ep + ab + ru + ilm + H_2O at low temperature conditions. The garnet-in reactions appear at high pressure conditions (> 6.5 kbar) in the temperature range 525–720 °C. Gedrite-bearing fields appear in the pressure range 5–9.6 kbar and temperature range 600–790 °C. The cordierite-bearing assemblages appear at low pressure conditions and high temperature (> 600 °C) conditions. The orthopyroxene-in reactions appear as isothermal boundaries at 765 °C. At high pressure conditions (> 6.5 kbar), the orthopyroxene-in reactions appears at > 800 °C. The melting reactions appear as isothermal reactions (~700–720 °C). The chlorite-bearing fields are stable at different pressure conditions but at low temperature (< 590 °C). On the other hand, albite is stable at the same pressure as chlorite but at much lower temperature (< 410–530 °C).

The metamorphic peak is constrained by the assemblage bi + g + pl + ilm + liq on Fig. 7b. The X_{Fe}^{g}, Z(g) isopleths and liquid modes were added to the field of the peak assemblage to determine the peak conditions. The Z(g) is 0.04–0.0445 implying that the peak pressure is 7.7–8.2 kbar. The X_{Fe}^{g} ranges between 0.71 and 0.72, this indicates that sample F93d reached peak conditions at 690–715 °C. This is consistent with P–T estimates obtained from conventional thermobarometers as discussed above. The intersections of the X_{Fe}^{g} and Z(g) isopleths support the assumption that the liquid mode of the rock is not more than 5%. The presence of cordierite and the absence of orthopyroxene and gedrite indicate that sample F93d re-equilibrated at low pressure–high temperature conditions (< 6 kbar, 600–760 °C). Unfortunately, mineral isopleths of the assemblage bi + cd + pl + ilm + H_2O are more or less isothermal which means that the temperature can be determined. Y(bi) reveals that sample F93d re-equilibrated at a temperature range 650–700 °C. Low temperature retrograde conditions could be identified by the presence of late chlorite and rutile and the absence of epidote and albite. The compositions of the late chlorite and late biotite constrains the retrograde P–T conditions to 3.5–4.8 kbar and 465–500 °C (Fig. 7c).

DISCUSSION

The pseudosections discussed above constrain different metamorphic conditions in different rock types (Figs 6 & 7). In this section, we discuss if these different conditions reflect separate events or whether they can be connected to a path for a single orogenic cycle. This path is then related to the deformation history and an integrated P–T–D evolution for the FSMC is derived. It is also discussed as to why different rock types record different stages of the evolution.

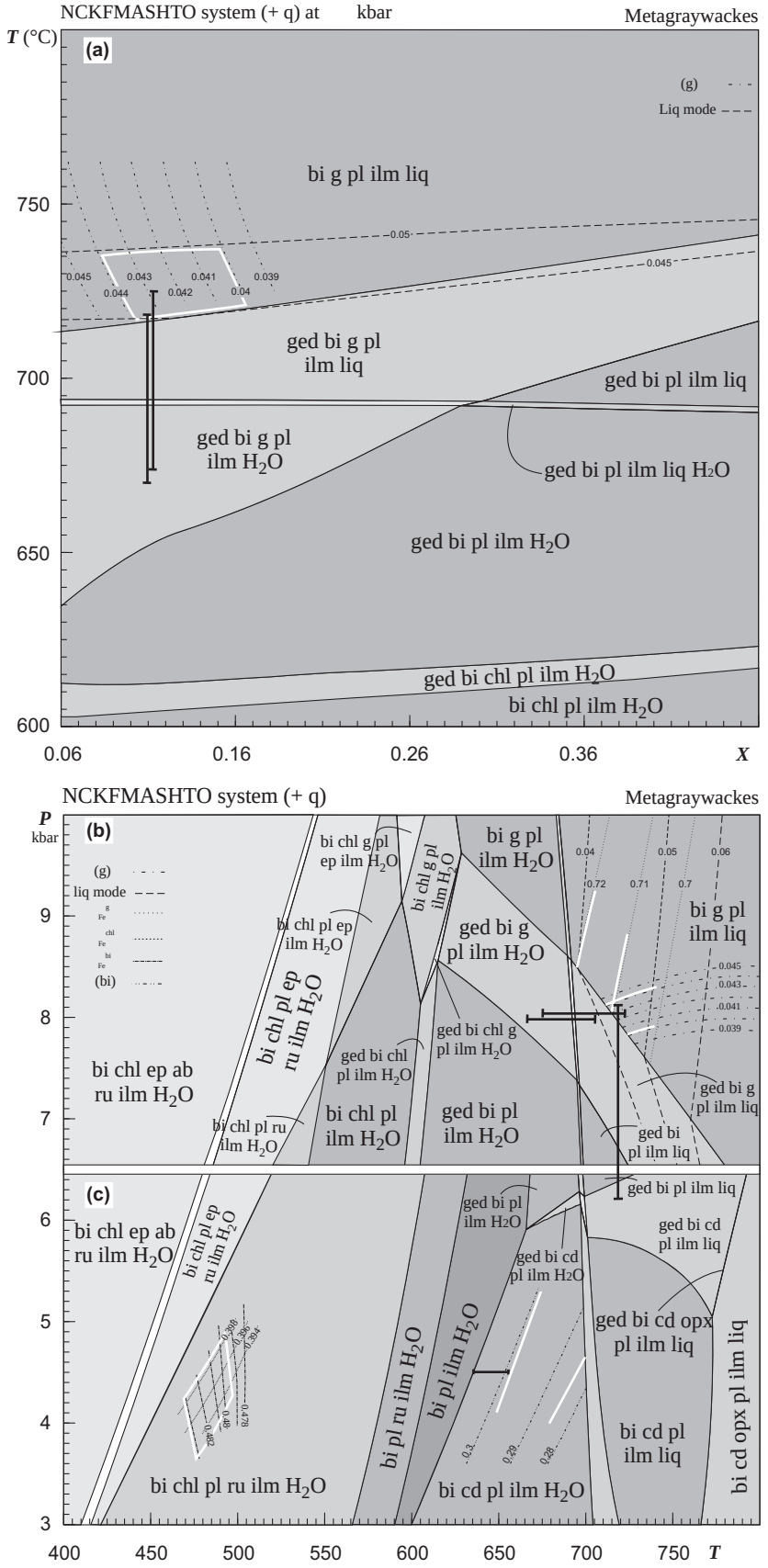

Fig. 7. *P–T* and *T–X*o pseudosections for the metagraywackes (sample F93d). (a) *T–X*o pseudosection. The bulk composition is that derived from XRF analysis (mol.%): SiO_2: 66.41, Al_2O_3: 9.4, CaO: 2.35, MgO: 8.14, FeO: 8.14, Na_2O: 2.48, K_2O: 2.19, TiO_2: 0.79, H_2O: 5.41 (Table 3). (b) *P–T* pseudosection at high pressure conditions using the bulk composition derived from (a) with *X*o: 0.13. (c) *P–T* pseudosection at low pressure conditions using the bulk composition of (b) from which 80% of the garnet was removed (mol.%; SiO_2: 64.35, Al_2O_3: 8.48, CaO: 2.25, MgO: 7.5, FeO: 5.04, Na_2O: 2.53, K_2O: 2.23, TiO_2: 0.81, H_2O: 5.51). The vertical and the horizontal bars are the average *P* and *T* according to the garnet–biotite–plagioclase thermobarometers (Table 2) and the garnet–cordierite thermometer.

P–T path and its relationship to deformation

In summary from above, pre-metamorphic peak conditions are constrained by the chemistry of clinopyroxene and plagioclase (and the absence of magnetite) in the migmatites. These pre-peak conditions are ~550–620 °C and 7.2–8.2 kbar. Peak metamorphic conditions derived for the metagraywackes are ~690–715 °C and 7.7–8.2 kbar (Fig. 7). In the migmatites, the peak is constrained at a similar pressure, but temperatures ~660–775 °C (Fig. 6a). The somewhat higher peak temperatures may simply reflect that the migmatites (located in the core of the FSMC) were located at slightly deeper crustal levels at the time of peak metamorphism. However, it is also important to note that the peak conditions of the migmatites were derived without considering a melt model for this bulk composition so that they are subject to some uncertainly. Peak assemblages in both the migmatites and the metagraywackes are overprinted by later parageneses that equilibrated at ~645–700 °C and 4.7–5.3 kbar. Finally, all studied samples give petrographical and mineral chemical indications for partial re-equilibration at low pressure–low temperature conditions of ~460–530 °C and ~4–5 kbar.

Interestingly, the metamorphic peak recorded by the migmatites and metagraywackes is not preserved in the hornblende gneisses. The coarse-grained peak assemblage in the hornblende gneisses (hb + pl + ilm + mt) formed at ~630–770 °C and < 5.3 kbar. These conditions correspond to the post-peak assemblage in the other rock types. The final isobaric cooling is recorded in all rock types. We suggest that the migmatites and hornblende gneisses record different stages of the *P–T* path and interpret this as a reflection of the water content of the rocks: in the migmatites, water was partitioned into the melt at the metamorphic peak, causing a relative dry residue assemblage and thus preservation of the peak assemblage (e.g. White & Powell, 2002). Conversely, the paragneisses around the granitic dykes are enriched in K-feldspar which indicate metasomatic infiltration. In addition all the metamorphic rocks around the migmatites were affected by complex fluid-infiltration processes after the peak metamorphism (Abu-Alam & Stüwe, Unpublished data). We interpret therefore that the hornblende gneisses had sufficient water during their entire evolution so that later equilibration along the same *P–T* path of the migmatites and metagraywackes was possible (e.g. Guiraud *et al.*, 2001).

The different metamorphic conditions described here were interpreted by El-Shafei & Kusky (2003) as evidence for two discrete metamorphic events: a medium grade event M_1 (recorded by the hornblende gneisses) and a high-grade M_2 event associated with the formation of migmatites. However, Fowler & Hassan (2008) suggested only one metamorphic event. Textural, microstructural and thermobarometric evidence presented here is agreement with Fowler & Hassan (2008) and suggests that minor grade variations can be interpreted in terms of structural level and different rock types. We infer therefore that the pre-peak-, peak- and retrograde conditions reflect the partial record of a single continuous 'clockwise' *P–T* path. This interpretation is consistent with geochronological and tectonic evidence from elsewhere in the Arabian-Nubian shield (Abu El-Enen *et al.*, 2004; Eliwa *et al.*, 2008). Then, the inferred *P–T* path is characterized by heating with moderate burial at mid crustal levels (for an overburden density 2850 kg m^{-3} and assuming lithostatic conditions the peak metamorphic conditions corresponds to a depth of 25.7–29.3 km) followed by isothermal decompression because of rapid exhumation to ~5 kbar and final cooling to stable geothermal conditions at this depth (~14.3–17.9 km). The final isobaric cooling path is consistent with observations in Taba metamorphic complex (the nearest high-grade metamorphic complex) where final cooling is also near isobaric at ~4.5–5 kbar (Abu El-Enen *et al.*, 2004). Exhumation from this depth (~14.3–17.9 km) to the surface is not recorded by the metamorphic parageneses and will be interpreted below.

The *P–T* evolution can now be correlated with the four deformation phases that affected the Feiran–Solaf region (Fig. 8). All peak parageneses grew in the S_1 foliation as well as the presence of leucosomes which are parallel and cross-cutting to the principal foliation suggesting that peak metamorphism was syn- or just post-D_1 (Fig. 8). This interpretation is in agreement with the observations of Fowler & Hassan (2008) in the Feiran complex, but we note that it is different from other metamorphic complexes in Sinai: in Taba and Elat metamorphic complexes, Cosca *et al.* (1999) suggested that the peak metamorphism was associated with three ductile deformation phases D_1–D_3, while Abu El-Enen *et al.* (2004) suggested that the peak metamorphism associated with D_2.

However, we note that D_2 in Taba may correspond to D_1 in the FSMC as we have found sparse evidence for a deformation phase prior to peak metamorphism. Microstructural evidence and field evidence shows that D_2 and D_3 are compressive deformation phases. Thus, these deformation phases must have occurred during the isothermal decompression and/or subsequent cooling. As D_2 and D_3 structures are in places cut by leucosomes, these phases are likely to have occurred during the decompression phase above the solidus (Fig. 8). In the Taba, Kid and Elat metamorphic complexes, the D_2 and D_3 phases are also recorded as ductile phases (e.g. Cosca *et al.*, 1999; Abu El-Enen *et al.*, 2003, 2004; Eliwa *et al.*, 2008) but their relationship to the decompression path has not been documented. On D_4 there are no direct constraints. We suggest that it either occurred during cooling or during the exhumation post-date to the 4 kbar cooling documented here.

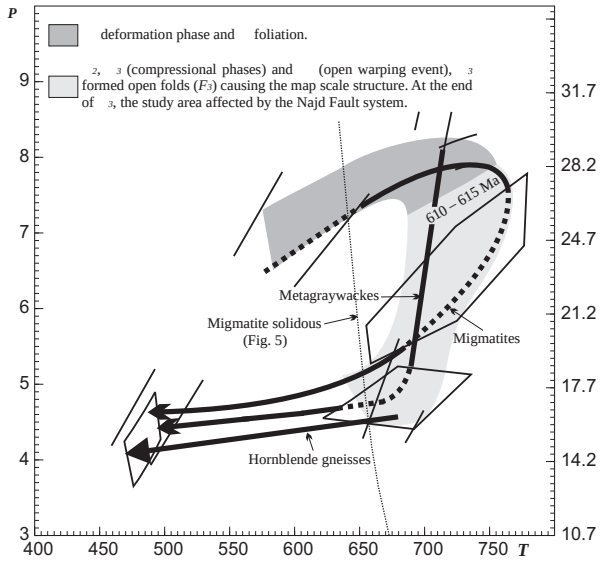

Fig. 8. Summary of the *P–T* paths of metagraywackes, hornblende gneisses and migmatites. The thick arrows mark the *P–T* paths. The lines and the polygons are the stability fields of the mineral assemblages from Figs 6 & 7.

The interpreted *P–T–D* evolution raises a series of problems of both conceptual and regional relevance that are now discussed. In particular, we discuss (i) the counter-intuitive synchronous occurrence of isothermal decompression (recorded by the parageneses and suggested exhumation) and convergent deformation phases (recorded by field evidence and suggested burial) and (ii) the tectonic relevance of the documented evolution.

Exhumation during compressive deformation

The observation of synchronous decompression and convergent deformation phases is not unique to the FSMC. Carson *et al.* (1997) observed a similar relationship in the Larsemann Hills in Antarctica and in several other high-grade complexes convergence is observed synchronously with the decompression phase of the *P–T* path. For the Larsemann Hills, Carson *et al.* (1997) suggested that it reflects rapid upper crustal extension at the time of lower crustal convergence. However, for the FSMC the model of Carson *et al.* (1997) is unsatisfactory, as the region is a relatively small area for which orogen scale considerations may not apply. In a more simple, one-dimensional interpretation, Stüwe & Barr (1998) showed that simultaneous erosion and convergence will result in a deformation field characterized by decompression during convergence above a critical point in the crust and burial below that. This critical point separates an upper part of the crust where upwards advection by erosion outweighs convergence from a lower part where deformation outweighs erosion. The depth of this critical point depends on the relative rates of erosion and deformation but can be as deep as ~30 km. Because the FSMC records decompression from ~29 km, this model may, in principal, be a possible explanation. However, here we suggest that the synchronous occurrence of convergent deformation and decompression is simply a reflection of a complicated obliquely convergent geometry of the D_2 and D_3 events which caused exhumation in a wrench system. Within this wrench system overall convergence was accompanied by extrusion of the complex to the surface. Such a wrench system is well known from the Pan-African basement in Sinai and the Eastern Desert: the Najd fault system.

Tectonic implications in the context of the Najd fault system

The lithosphere-scale Najd fault system (Fig. 1) is known to be related to the exhumation history of a series of high-grade metamorphic terranes throughout the Eastern Desert of Egypt and Sinai that are of similar age and grade to the FSMC (615–610 Ma; Stern & Manton, 1987): Pan-African metamorphic areas are known for example in Wadi Hafafit (620–580 Ma, Abd El-Naby *et al.*, 2008; Loizenbauer *et al.*, 2001; Stern & Hedge, 1985; Hashad *et al.*, 1981), Taba complex (605 Ma, Eliwa *et al.*, 2008), Meatiq metamorphic core complex (640–580 Ma, Fritz *et al.*, 1996, 2002; Loizenbauer *et al.*, 2001; Stern & Hedge, 1985) and Sibai dome (614 Ma, Fritz *et al.*, 1996, 2002). All of these regions are characterized by low pressure–high temperature peak conditions ~6–8.5 kbar and 600–750 °C comparable with those described here (e.g. Loizenbauer *et al.*, 2001; Abd El-Naby *et al.*, 2008; Eliwa *et al.*, 2008). Interestingly, most of the terranes in the Eastern Desert were exhumed as core complexes in extensional environments, while we interpret the FSMC to have exhumed in an overall regime of compression.

Here, it is argued that both mechanisms are possible within the overall setting of the Najd fault system: this fault system has a general NW–SE orientation (with substantial local variation, see e.g. Shalaby *et al.*, 2006) and a sinistral motion, so that the maximum compressive stress is oriented roughly W–E. We suggest that minor variation in the orientation of the various metamorphic complexes with respect to the Najd fault system boundaries cause the different exhumation mechanisms: in the Eastern Desert, the intermediate principal stress may be oriented vertically causing overall extension, while in the FSMC the minimum principal stress is vertical causing exhumation in an overall horizontal transpressive regime (Fig. 1). We therefore suggest that the Najd fault system (D_3 in the FSMC) is the principal phase causing the exhumation of the complex in an oblique transpressive regime (Fig. 9). Within this setting, major volumes of post-tectonic granites that surround the complex were produced by decompression-enhanced melting and are transported through the Najd fault system, thereby

obliterating the margins of the complex. Our interpretation is nicely consistent with interpretations from the Eastern Desert where the D_3 phase is also interpreted as the Najd Fault system and related to ascent of the post-tectonic granitic magma (e.g. Shalaby *et al*., 2005; Farahat *et al*., 2007).

Final exhumation to the surface

An interesting and as yet unresolved aspect of the tectonic evolution of the FSMC is its final exhumation to the surface. This study has inferred a metamorphic evolution that terminates at ~450 °C and ~15 km depth suggesting that the final exhumation must be related to an independent event. Interestingly, this depth is roughly the peak metamorphic depth of the low-grade metamorphic belts in Sinai (Ayalon *et al*., 1987; Eliwa *et al*., 2004) suggesting that these belts were not affected by the Najd fault system. Zircon and apatite fission track thermochronometers indicate that the study area was subject to a complex history of exhumation and reburial from the Cambrian to the Early Tertiary period (e.g. Kohn *et al*., 1992). However, Vermeesch *et al*. (2009) suggested that the calcalkaline rocks (at the same crustal level of the high-grade gneisses) were exposed by c. 590 Ma suggesting that the final exhumation occurred already at the end of the Pan-African. In fact, in the FSMC, the presence of an unconformity between gneisses and a Cretaceous succession and the absence of the pre-Cretaceous sedimentary cover (Fig. 2) suggest that the study area was exhumed and subjected to intense pre-Cretaceous erosion prior to being reburied under the Cretaceous succession. This implies that the final exhumation of the FSMC from ~15 km occurred in an event following the Pan-African high-grade evolution. Such an event has not been described, but there is sedimentary evidence from the Hammamat molasse that subsidence occurred and basins formed at *c*. 585 ± 15 Ma (Willis *et al*., 1988). Within this event the lower-grade metamorphic belts of Sinai, like the Sa'al belt, may also have exhumed.

CONCLUSIONS

In conclusion, the following tectonic evolution is inferred from our study (Fig. 9). The rocks of the Wadi Feiran belt include a series of metasedimentary and metavolcanic rock types with minor mafic intercalations and calc-silicates that are consistent with an interpretation as a sedimentary succession in a marginal basin between Pan-African volcanic arcs (El-Gaby & Ahmed, 1980). Vertical flattening (Fowler & Hassan, 2008) was associated with horizontal

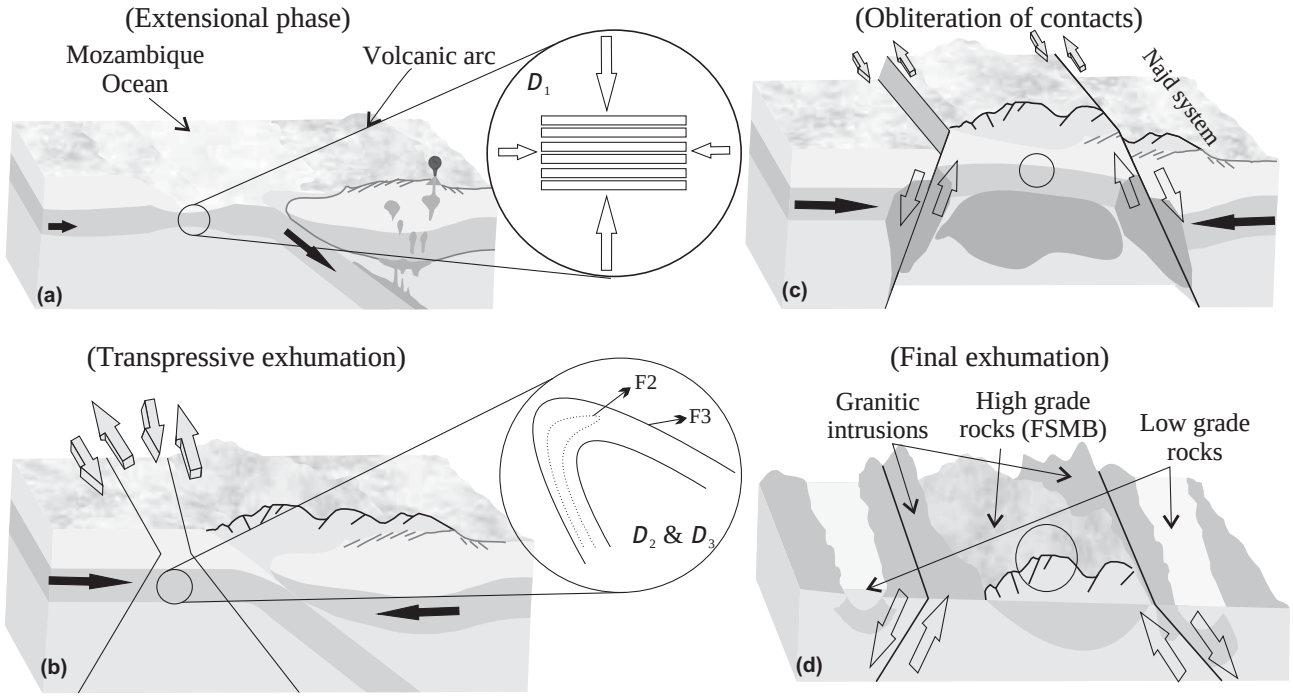

Fig. 9. Tectono-metamorphic model of Wadi Feiran Solaf metamorphic complex during the Pan-African event. (a) Igneous activity formed volcanic arcs and related intrusive rocks (632 ± 3) Ma. Immature sediments were deposited in a marginal basin, followed by D_1 deformation due to vertical flattening. (b) Due to the arc–arc accretions and the closing of the Mozambique Ocean, the D_2 and D_3 compressional phases occurred. (c) At the end of D_3, the study area was exhumed by oblique compressive deformation associated with sinistral strike–slip shear zone to the depth of 14.3–17.9 km. (d) The present day situation. The solid circles are the position of the FSMC during the evolution.

transport towards the west and north-west, forming the penetrative S_1 foliation and causing burial of the rocks. The rocks reached peak metamorphism ~7.2–8.2 kbar and 645–775 °C at 610–615 Ma towards the end of D_1 and prior to D_2. The subsequent D_2 and D_3 deformation phases caused shortening in NE–SW direction at the time of substantial near isothermal decompression of the rocks. The D_3, phase is correlated with the sinistral NW–SE striking Najd fault system and exhumed the complex in an oblique transpressive regime. We suggest that the difference between the transpressive exhumation interpreted here and the extensional core complexes of the Eastern Desert is a consequence of minor variation of the orientation of the various belts with respect to the Najd fault system. Because of the rapid exhumation, large volumes of post-tectonic granitic magma was formed and transported along the Najd fault system into the complex thereby obliterating most of its margins. The doming up of the entire complex and the NE–SW F_4 were formed by the open warping event (D_4) which was possibly related to the final exhumation from ~15 km depth to the surface during an independent event.

ACKNOWLEDGEMENTS

This project was supported by the Austria exchange service (ÖAD) scholarship. We thank F. Makroum, A. Shalaby, M. El-Shafei and Y.M. Sultan for their help during the field work. Help with the pseudosections by V. Tenczer is appreciated. C. Hauzenberger is thanked for his help with the XRF analysis. R.J. Stern is thanked for his help with inaccessible papers. S. Boger and M. Abu El-Enen are thanked for their constructive reviews. R. White is appreciated for his constructive suggestions and efficient editorial handling of the manuscript.

REFERENCES

Abd El-Naby, H., Frisch, W. & Siebel, W., 2008. Tectono-metamorphic evolution of the Wadi Hafafit Culmination (central Eastern Desert, Egypt). Implication for Neoproterozoic core complex exhumation in NE Africa. *Geologica Acta*, **6,** 293–312.

Abdelsalam, M. G. & Stern, R. J., 1996. Sutures and shear zones in the Arabian-Nubian Shield. *Journal of African Earth Sciences*, **23,** 289–310.

Abu El-Enen, M. M., Okrusch, M. & Will, T. M., 2003. Metapelitic assemblages in the Umm Zariq schists, central western Kid Belt, Sinai Peninsula, Egypt. *Neues Jahrbuch Mineralogie Abhandlungen*, **178,** 277–306.

Abu El-Enen, M. M., Will, T. M. & Okrusch, M., 2004. *P–T* evolution of the Pan-African Taba metamorphic belt, Sinai, Egypt: constraints from metapelitic mineral assemblages. *Journal of African Earth Sciences*, **38,** 59–78.

Ahmed, A. A., 1981. Reconsidered view on Feiran–Solaf Gneisses southwest of Sinai, Egypt. *Bulletin Faculty of Sciences, Assiut University*, **10,** 131–142.

Ahmed, A. A. & Youssef, M. M., 1976. Air photo interpretation of dike swarms in the area around Feiran Oasis, southwest Sinai, Egypt. *Bulletin Faculty of Sciences, Assiut University*, **1,** 1–17.

Ayalon, A., Steinitz, G. & Starinsky, A., 1987. K–Ar and Rb–Sr whole-rock ages reset during Pan-African event in the Sinai Peninsula (Ataqa Area). *Precambrian Research*, **37,** 191–197.

Bhattacharya, A., Mohanty, L., Maji, A., Sen, S. K. & Raith, M., 1992. Non-ideal mixing in the phlogopite–annite binary: constraints from experimental data on Mg–Fe partitioning and a reformulation of the biotite–garnet geothermometer. *Contributions to Mineralogy and Petrology*, **111,** 87–93.

Blasband, B., Brooijmans, P., Dirks, P., Visser, W. & White, S., 1997. A Pan-African core complex in the Sinai, Egypt. *Geologie en Mijnbouw*, **76,** 247–266.

Blasband, B., White, S., Brooijmans, P., De Brooder, H. & Visser, W., 2000. Late Proterozoic extensional collapse in Arabian-Nubian Shield. *Journal of the Geological Society, London*, **157,** 615–628.

Blundy, J. & Holland, T., 1990. Calcic amphibole equilibria and a new amphibole plagioclase geothermometer. *Contributions to Mineralogy and Petrology*, **104,** 208–224.

Brooijmans, P., Blasband, B., White, S. H., Visser, W. J. & Dirks, P., 2003. Geothermobarometric evidence for a metamorphic core complex in Sinai, Egypt. *Precambrian Research*, **123,** 249–268.

Carson, C. J., Powell, R., Wilson, C. J. L. & Dirks, P. H. M. G., 1997. Partial melting during tectonic exhumation of a granulite terrane: an example from the Larsemann Hills, East Antractica. *Journal of Metamorphic Geology*, **15,** 105–126.

Coggon, R. & Holland, T. J. B., 2002. Mixing properties of phengitic micas and revised garnet–phengite thermobarometers. *Journal of Metamorphic Geology*, **20,** 683–696.

Cosca, M. A., Shimron, A. & Caby, R., 1999. Late Precambrian metamorphism and cooling in the Arabian-Nubian Shield: petrology and $^{40}Ar/^{39}Ar$ geochronology of metamorphic rocks of the Elat area (southern Israel). *Precambrian Research*, **98,** 107–127.

Dachs, E., 2004. PET: petrological elementary tools for mathematica: an update. *Computers and Geosciences*, **30,** 173–182.

Diener, J. F. A., Powell, R., White, R. W. & Holland, T. J. B., 2007. A new thermodynamic model for clino- and orthoamphiboles in the system Na_2O–CaO–FeO–MgO–Al_2O_3–SiO_2–H_2O–O. *Journal of Metamorphic Geology*, **25,** 631–656.

El-Gaby, S. & Ahmed, A. A., 1980. The Feiran–Solaf gneiss belt, SW of Sinai, Egypt. In: *Evolution and Mineralization of the Arabian-Nubian Shield* (eds Coory, P.G. & Tahoun, S.A.). *Institute of Applied Geology*, **4,** 95–105, Jeddah.

El-Gaby, S., List, F. K. & Tehrani, R., 1990. The basement complex of the Eastern Desert and Sinai. In: *The Geology of Egypt* (ed. Rushdi, S.), pp. 175–184. Balkema, Rotterdam.

Eliwa, H. A., Abu El-Enen, M. M., Khalaf, I. & Itaya, T., 2004. Metamorphic evolution of Sinai metapelites and gneisses: constrains from petrology and K/Ar age dating. *Egyptian Journal of Geology*, **48,** 169–185.

Eliwa, H. A., Abu El-Enen, M. M., Khalaf, I. M., Itaya, T. & Murata, M., 2008. Metamorphic evolution of Neoproterozoic metapelites and gneisses in Sinai, Egypt: insights from petrology, mineral chemistry and K–Ar age dating. *Journal of African Earth Sciences*, **51,** 107–122.

El-Shafei, M. K. & Kusky, T. M., 2003. Structural and tectonic evolution of the Neoproterozoic Feiran–Solaf metamorphic belt, Sinai Peninsula: implications for the closure of the Mozambique Ocean. *Precambrian Research*, **123,** 269–293.

El-Tokhi, M., 1992. Origin and tectonic implications of Pan-African amphibolites of Wadi Feiran South Sinai. In: *Proceedings of the Third Conference on Geology of Sinai Development* (eds Abd El-Khalek, M. L., El-Ghawaby, M. A. & Morsy, A. M.). Suez Canal University pp. 239–248. Ismailia.

Engel, A. E. J., Dixon, T. H. & Stern, R. J., 1980. Late Precambrian evolution of Afro-Arabian crust from ocean to craton. *Geological Society America Bulletin*, **91,** 699–706.

Farahat, E. S., Mohamed, H. A., Ahmed, A. F. & El Mahallawi, M. M., 2007. Origin of I- and A-type granitoids from the Eastern Desert of Egypt: implications for crustal growth in the northern Arabian-Nubian Shield. *Journal of African Earth Sciences*, **49,** 43–58.

Fowler, A. & Hassan, I., 2008. Extensional tectonic origin of gneissosity and related structures of the Feiran–Solaf metamorphic belt, Sinai, Egypt. *Precambrian Research*, **164,** 119–136.

Fritz, H., Wallbrecher, E., Khudeir, A. A., Abu El Ela, F. & Dallmeyer, D. R., 1996. Formation of Neoproterozoic metamorphic core complexes during oblique convergence (Eastern Desert, Egypt). *Journal of African Earth Sciences*, **23,** 311–323.

Fritz, H., Dallmeyer, D. R., Wallbrecher, E. *et al*., 2002. Neoproterozoic tectonothermal evolution of the Central Eastern Desert, Egypt: a slow velocity tectonic process of core complex exhumation. *Journal of African Earth Sciences*, **34,** 137–155.

Ganguly, J. & Saxena, S. K., 1984. Mixing properties of aluminosilicate garnets: constraints from natural and experimental data, and applications to geothermo-barometry. *American Mineralogist*, **69,** 88–97.

Gass, I. G., 1982. Upper Proterozoic (Pan-African) calcalkaline magmatism in northeastern Africa and Arabia. In: *Andesites* (ed. Thorpe, R.S.), pp. 591–609. Wiley, New York.

Green, E. C. R., Holland, T. J. B. & Powell, R., 2007. An order-disorder model for omphacitic pyroxenes in the system jadeite–diopside–hedenbergite–acmite, with applications to eclogitic rocks. *American Mineralogist*, **92,** 1181–1189.

Guiraud, M., Powell, R. & Rebay, G., 2001. H_2O in metamorphism and unexpected behaviour in the preservation of metamorphic mineral assemblages. *Journal of Metamorphic Geology*, **19,** 445–454.

Hashad, A. H., Sayyah, T. A. & El Manharawy, M. S., 1981. Isotopic composition of strontium and origin of Wadi Kareim volcanics, Eastern Desert. *Egyptian Journal of Geology*, **25,** 141–147.

Hoisch, T., 1990. Empirical calibration of six geobarometers for the mineral assemblage quartz + muscovite + biotite + plagioclase + garnet. *Contributions to Mineralogy and Petrology*, **104,** 225–234.

Holland, T. J. B. & Powell, R., 1998. An internally consistent thermodynamic dataset for phases of petrological interest. *Journal of Metamorphic Geology*, **16,** 309–343.

Holland, T. J. B. & Powell, R., 2003. Activity–composition relations for phases in petrological calculations: an asymmetric multicomponent formulation. *Contributions to Mineralogy and Petrology*, **145,** 492–501.

Holland, T. J. B., Baker, J. M. & Powell, R., 1998. Mixing properties and activity–composition relationships of chlorites in the system $MgO–FeO–Al_2O_3–SiO_2–H_2O$. *European Journal of Mineralogy*, **10,** 395–406.

Johnson, P. R., 1998. Tectonic map of Saudi Arabia and adjacents areas (scale: 1/4,000,000). In: Technical report USGSOF-98-3 (ed. Saudi Arabian Deputy Ministry for Mineral Resources), 2pp. Saudi Arabia, Jeddah.

Johnson, T. E., White, R. W. & Powell, R., 2008. Partial melting of metagreywacke: a calculated mineral equilibria study. *Journal of Metamorphic Geology*, **26,** 837–853.

Katz, O., Beyth, M., Miller, N. *et al*., 2004. A Late Neoproterozoic ($\sim$ 630 Ma) high-magnesium andesite suite from south Israel: implications for the consolidation of Gondwanaland. *Earth and Planetary Science Letters*, **218,** 475–490.

Khudeir, A. A., Abu El-Rus, M. A., El-Gaby, S., El-Nady, O. & Bishara, W. W., 2008. Sr–Nd isotopes and geochemistry of the infrastructural rocks in the Meatiq and Hafafit core complexes, Eastern Desert, Egypt: evidence for involvement of Pre-Neoproterozoic crust in the growth of Arabian-Nubian Shield. *Island Arc*, **17,** 90–108.

Kohn, B. P., Eyal, M. & Feinstein, S., 1992. A major late Devonian-early Carboniferous (Hercynian) thermotectonic event at the new margin of the Arabian-Nubian Shield: evidence from zircon fission track dating. *Tectonics*, **11,** 1018–1027.

Kröner, A., 1984. Late Precambrian plate tectonics and orogeny: a need to redefine the term Pan-African. In: *Géologie Africaine* (eds Klerkx, J. & Michot, J.), pp. 23–28. Musée Royal de l'Afrique Centrale, Tervuren.

Kröner, A., Krüger, J. & Rashwan, A. A., 1994. Age and tectonic setting of granitoid gneisses in the Eastern Desert of Egypt and south-west Sinai. *Geologische Rundschau*, **83,** 502–513.

Le Maitre, R. W., 1976. The chemical variability of some common igneous rocks. *Journal of Petrology*, **17,** 589–637.

Leake, B. E., Woollet, A. R., Arps, C. E. *et al*., 1997. Nomenclature of amphiboles: report of the subcommittee on amphiboles of the International Mineralogical Association, commission on new minerals and mineral names. *American Mineralogist*, **82,** 1019–1037.

Loizenbauer, J., Wallbrecher, E., Fritz, H., Neumayr, P., Khudeir, A. A. & Kloetzli, U., 2001. Structural geology, single zircon ages and fluid inclusion studies of the Meatiq metamorphic core complex: implications for Neoproterozoic tectonics in the Eastern Desert of Egypt. *Precambrian Research*, **110,** 357–383.

Mahar, E. M., Baker, J. M., Powell, R., Holland, T. J. B. & Howell, N., 1997. The effect of Mn on mineral stability in metapelites. *Journal of Metamorphic Geology*, **15,** 223–238.

Morimoto, M., 1988. Nomenclature of pyroxenes. *Mineralogical Magazine*, **52,** 535–550.

Perchuk, L. L. & Lavrent'eva, I. V., 1983. Experimental investigation of exchange equilibria in the system cordierite–garnet–biotite. In: *Kinetics and Equilibrium in Mineral Reactions* (ed. Saxena, S.K.), pp. 199–239. Springer Verlag, New York.

Powell, R. & Holland, T. J. B., 1988. An internally consistent thermodynamic dataset with uncertainties and correlations: 3. Application, methods, work examples and a computer program. *Journal of Metamorphic Geology*, **6,** 173–204.

Rasse, P., 1974. Al and Ti contents of hornblende, indicators of pressure and temperature of regional metamorphism. *Contributions to Mineralogy and Petrology*, **45,** 231–236.

Sawyer, E. W., 1986. The influence of source rock type, chemical weathering and sorting on the geochemistry of clastic sediments from the Quetico metasedimentary belt, Superior Province, Canada. *Chemical Geology*, **55,** 77–95.

Sawyer, E. W., 1999. Criteria for the recognition of partial melting. *Physics and Chemistry of the Earth*, **24,** 269–279.

Shalaby, A., Stüwe, K., Makroum, F., Fritz, H., Kebede, T. & Klötzli, U., 2005. The Wadi Mubarak belt, Eastern Desert: a Neoproterozoic conjugate shear system in the Arabian-Nubian Shield. *Precambrian Research*, **136,** 27–50.

Shalaby, A., Stüwe, K., Fritz, H. & Makroum, F., 2006. The El Mayah molasse basin in the Eastern Desert of Egypt. *Journal of African Earth Sciences*, **45,** 1–15.

Stern, R. J. & Hedge, C. E., 1985. Geochronologic and isotopic constraints on Late Precambrian crustal evolution in the Eastern Desert of Egypt. *American Journal of Sciences*, **285,** 97–127.

Stern, R. J. & Manton, W. I., 1987. Age of Feiran basement rocks, Sinai: implications for late Precambrian crustal evolution in the northern Arabian-Nubian Shield. *Journal of the Geological Society, London*, **144,** 569–578.

Stern, R. J. & Manton, W. I., 1988. Discussion on the age of Feiran basement rocks, Sinai: implications for late Precambrian crustal evolution in the northern Arabian-Nubian Shield. *Journal of the Geological Society, London*, **145,** 1033–1035.

Stüwe, K., 1997. Effective bulk composition changes due to cooling: a model predicting complexities in retrograde reaction textures. *Contributions to Mineralogy and Petrology*, **129,** 43–52.

Stüwe, K. & Barr, T. D., 1998. On uplift and exhumation during convergence. *Tectonics*, **17,** 80–88.

Thompson, J. B., 1976. Mineral reactions in pelitic rocks; II, Calculation of some *P–T*–X (Fe–Mg) phase relations. *American Journal of Science*, **276,** 425–454.
Vermeesch, P., Avigad, D. & McWilliams, M. O., 2009. 500 Myr of thermal history elucidated by multi-method detrital thermochronology of North Gondwana Cambrian sandstone (Eilat area, Israel). *Geological Society of America Bulletin*, **121,** 1204–1216.
Vernon, R. H., 2004. *A Practical Guide to Rock Microstructure*. Cambridge University Press, Cambridge, 594 pp.
White, R. W. & Powell, R., 2002. Melt loss and the preservation of granulite facies mineral assemblages. *Journal of Metamorphic Geology*, **20,** 621–632.
White, R. W., Powell, R., Holland, T. J. B. & Worley, B. A., 2000. The effect of TiO_2 and Fe_2O_3 on metapelitic assemblages at greenschist and amphibolite facies conditions: mineral equilibria calculation in the system K_2O-FeO-MgO-Al_2O_3-SiO_2-H_2O-TiO_2-Fe_2O_3. *Journal of Metamorphic Geology*, **18,** 497–511.
White, R. W., Powell, R. & Clarke, G. L., 2002. The interpretation of reaction textures in Fe-rich metapelitic granulites of the Musgrave Block, central Australia: constraints from mineral equilibria calculations in the system K_2O–FeO–MgO–Al_2O_3–SiO_2–H_2O–TiO_2–Fe_2O_3. *Journal of Metamorphic Geology*, **20,** 41–55.
White, R. W., Powell, R. & Holland, T. J. B., 2007. Progress relating to calculation of partial melting equilibria for metapelites. *Journal of Metamorphic Geology*, **25,** 511–527.
Willis, K. M., Stern, R. J. & Clauer, N., 1988. Age and geochemistry of Late Precambrian sediments of the Hammamat series from Northeastern Desert of Egypt. *Precambrian Research*, **42,** 173–187.

SUPPORTING INFORMATION

Additional Supporting Information may be found in the online version of this article:

Table S1. Representative amphibole analyses of sample F39 (migmatite) (numbers of ions on the basis of 23 O, ignoring H_2O).

Table S2. Representative plagioclase analyses of sample F39 (migmatite). The chemical formula based on 8 O.

Table S3. Representative cpx analyses of the assemblage (hb + di + pl + sph) sample F39 (migmatite). The chemical formula based on 6 O.

Table S4. Representative amphibole analyses of samples F1 and F63 (hornblende gneisses) (numbers of ions on the basis of 23 O, ignoring H_2O).

Table S5. Representative biotite analyses of sample F93 (metagraywacke) (numbers of ions on the basis of 11 O, ignoring H_2O).

Table S6. Representative chlorite analyses of sample F93 (metagraywacke) (numbers of ions on the basis of 14 O, ignoring H_2O).

Table S7. Representative garnet, biotite and plagioclase analyses of sample F93 (metagraywacke). The chemical formula based on, 11 O, ignoring H_2O for the biotite, 12 O for the garnet and 8 O for the plagioclase.

Table S8. Representative garnet and cordierite analyses of sample F93 (metagraywacke). The chemical formula based on, 18 O, ignoring H_2O for the cordierite and 12 O for the garnet.

Please note: Wiley-Blackwell are not responsible for the content or functionality of any supporting materials supplied by the authors. Any queries (other than missing material) should be directed to the corresponding author for the article.

Received 31 October 2008; revision accepted 15 May 2009.